AFRL-AFOSR-VA-TR-2019-0155

Nonlinear Optical Signal Processing On Chip: A New Paradigm for Implementation of Optical Logic Functionality

Ali Adibi
GEORGIA TECH RESEARCH CORPORATION

03/07/2019
Final Report

Air Force Research Laboratory
AF Office Of Scientific Research (AFOSR)/ RTB1
Arlington, Virginia 22203
Air Force Materiel Command

REPORT DOCUMENTATION PAGE

Form Approved
OMB No. 0704-0188

PLEASE DO NOT RETURN YOUR FORM TO THE ABOVE ORGANIZATION.

1. REPORT DATE *(DD-MM-YYYY)*	2. REPORT TYPE	3. DATES COVERED *(From - To)*
07-03-2019	Final Report	1/9/2015-31/8/2018

4. TITLE AND SUBTITLE

Hybrid Nonlinear Optical Signal Processing on Chip: A New Paradigm for Implementation of Optical Logic Functionality

5a. CONTRACT NUMBER

5b. GRANT NUMBER

FA9550-15-1-0342

5c. PROGRAM ELEMENT NUMBER

6. AUTHOR(S)

Ali Adibi (PI), Ali A. Eftekhar (co-PI)

5d. PROJECT NUMBER

5e. TASK NUMBER

5f. WORK UNIT NUMBER

7. PERFORMING ORGANIZATION NAME(S) AND ADDRESS(ES)

Georgia Tech Research Corporation
505 10th Street
Atlanta, GA 30332-0415

8. PERFORMING ORGANIZATION REPORT NUMBER

9. SPONSORING/MONITORING AGENCY NAME(S) AND ADDRESS(ES)

AFOSR
801 N Randolph St.
Arlington VA 22203

10. SPONSOR/MONITOR'S ACRONYM(S)

11. SPONSOR/MONITOR'S REPORT NUMBER(S)

12. DISTRIBUTION/AVAILABILITY STATEMENT

Approved for public release; distribution unlimited

13. SUPPLEMENTARY NOTES

14. ABSTRACT

This program resulted in a solid framework for enabling on-chip nonlinear optical processing through realization of five solid material and device platforms with unique features, for the first time: 1) multi-layer Si/SiN/SiC material platform for nonlinear optics, quantum photonics, and optoelectronic applications (including the demonstration of the coupling modulator architecture for low-power wideband devices), 2) a hybrid material platform formed by integration of phase-change materials with Si/SiN for miniaturized ultra-low-power optoelectronic and nonlinear photonic devices, 3) a hybrid active material platform formed by integration of two-dimensional transition metal dichalcogenides with CMOS-compatible substrates with the possibility of forming lateral heterostructures through a simple annealing process for the formation of active and nonlinear devices, 4) an integrated photonic/phononic material and device platform for nonlinear devices based on combined acoustic and optical waves (e.g., SBS-based devices), and 5) an integrated material platform based on an engineered array of plasmonic nanostructures for sensing and nonlinear optics on chip. The research in this program resulted in over 20 journal papers, 25 conference papers, and 20 invited talks.

15. SUBJECT TERMS

Integrated nanophotonics, Nonlinear optical signal processing, Active photonic materials and devices, Nonlinear optical materials and devices

16. SECURITY CLASSIFICATION OF:			17. LIMITATION OF ABSTRACT	18. NUMBER OF PAGES	19a. NAME OF RESPONSIBLE PERSON
a. REPORT	b. ABSTRACT	c. THIS PAGE			Ali Adibi
U	U	U	UU	26	19b. TELEPHONE NUMBER *(Include area code)* (404)385-2738

Final Report to the
Air Force Office of Scientific Research (AFOSR)

Hybrid Nonlinear Optical Signal Processing on Chip: A New Paradigm for Implementation of Optical Logic Functionality

Georgia Institute of Technology

Principal Investigator:

Ali Adibi
Professor, School of Electrical and Computer Engineering,
Georgia Institute of Technology
Atlanta, GA 30332-0250
e-mail:adibi@ee.gatech.edu
Tel: (404) 385-2738
Fax: (404) 894-4641

I. Introduction

This report summarizes achievements in Dr. Adibi's research group at Georgia Institute of Technology under the program supported by grant number FA9550-15-1-0342. This report mainly covers major achievements from September 1, 2017 until August 31, 2018 with brief descriptions. Achievements in the previous years of the program are reported in the annual progress reports for similar periods ending in 2016 and 2017. *For brevity, only the details of the recent progress after the last report is presented here along with a short summary of the previous achievements.* Detailed information also can be found in the recent publications or can be directly requested from Dr. Adibi.

The goal of this AFOSR-supported research was to develop efficient, low-power, and high speed nonlinear photonic material and device platforms for nonlinear optical signal processing that could potentially enable the concept of optical logic. Considering the limited nonlinear response of the available CMOS-compatible materials (e.g., silicon (Si) and silicon nitride (SiN)) for integrated nanophotonic structures, realization of new material platforms and device architectures for realization of competent nonlinear devices with reasonable performance is an urgent need. This important fundamental task took most of the resources of this program. Consequently, ***the program resulted in a solid framework for enabling on-chip nonlinear optical processing using an arsenal of hybrid CMOS-compatible material platforms and a series of optimized device architectures.*** While the duration of the program did not allow the eventual formation of the "optical logic" structures, the findings of this program can go far beyond the logic concept and enable urgently needed *nonlinear integrated photonic structures for state-of-the-art applications like reservoir computing, neuromorphic computing, frequency comb generation, stimulated Brillouin scattering (SBS)-based structures for nonlinear signal processing and laser stabilization, nonlinear plasmonic and photonic sensing, and many others.* Indeed, over a period of three years, this program resulted in ***5 solid material and device platforms with unique features***, for the first time: 1) multi-layer Si/SiN/SiC (silicon carbide) material platform for nonlinear optics, quantum photonics, and optoelectronic applications (including the demonstration of the coupling modulator architecture for low-power wideband devices), 2) a hybrid material platform formed by integration of phase-change materials (PCMs) with Si/SiN for miniaturized ultra-low-power optoelectronic and nonlinear photonic devices (including the demonstration of bistability on-chip), 3) a hybrid active material platform formed by integration of two-dimensional transition metal dichalcogenides (2D TMDCs) with CMOS-compatible substrates (e.g., Si and SiN) with the possibility of forming lateral heterostructures through a simple annealing process for the formation of active and nonlinear devices (e.g. light emitters and detectors), 4) an integrated photonic/phononic material and device platform for nonlinear devices based on combined acoustic and optical waves (e.g., SBS-based devices), and 5) an integrated material platform based on an engineered array of plasmonic nanostructures for sensing and nonlinear optics on chip (including demonstration of second harmonic generation (SHG) and sensing of chiral molecules). In addition to the results of this program, each material/device platform can enable several new devices for a wide range of applications (some of them listed above). As such, this program was very productive in providing a solid framework for multiple new programs in the area of integrated photonics for active, passive, and nonlinear applications. ***The research in this program has resulted in over 20 journal papers (9 journal papers in 2018), 25 conference papers (11 in 2018), and 20 invited conference and seminar talks (9 In 2018)***. The list of the publications that resulted from this research program is included at Section III.

In the first two years of this program, we studied different fundamental nonlinear mechanisms, materials, and device platforms that enable efficient nonlinear optical signal processing platforms. During this period, we developed the infrastructure for the analysis, design, optimization, fabrication, and characterization of the envisioned materials and devices. This resulted in the development of different simulation tools, fabrication processes, material integration schemes, and characterization tools for

nonlinear integrated photonic materials and devices. The main challenge in the development of a photonic nonlinear signal processing platform, which can surpass the performance of the conventional signal processing architectures based on digital electronic approaches (in terms of processing speed and power consumption) is the lack of on-chip efficient nonlinear mechanisms/materials. Therefore, to overcome this fundamental challenge, a good portion of our effort in this program was focused on identifying and development of new nonlinear all-optical mechanisms and alternative material platforms, which can mitigate this challenge and enable next generation nonlinear photonic devices for signal processing. While we could not get to the full demonstration of a nonlinear processing device for nonlinear signal processing in this program, we believe that the long-term impact of the achievements of this fundamental research will considerably overwhelms the advantages of demonstration of nonlinear processing devices in conventional material platforms with mediocre performance measures (that do not surpass those of digital electronic signal processing approaches).

In addition to the completion of work on the material platforms in the first two years (especially the SBS-devices), we focused in the third year on two material and device platforms for nonlinear devices namely, 1) 2D TMDCs with lateral heterostructures for adding nonlinearity and active properties to integrated nanophotonics, and 2) integrated photonic devices with unprecedented performance based on SiC, which can enable more efficient nonlinear photonic devices and also provide prospects for development of the necessary building blocks for chip-scale quantum computing. These two platforms are discussed in details in the rest of this report while briefly discussing the completion of the work of the first two years (for which separate reports were submitted in earlier years).

II. Research Accomplishments

II.A. Overview of the continuation of the research from previous annual reports

Our research in this program has been focused on developing new platforms for low-power and fast nonlinear photonic devices, which can harbor the development of new nonlinear signal processing platforms. In this approach, our work has been focused on multiple facets aiming at developing new hybrid engineered material and device platforms and the study of their fundamental properties for enabling ultrafast, low-power, and miniaturized devices and systems for nonlinear signal processing on chip (e.g., for optical computing, frequency comb generation and manipulation, and digital logic).

Figure 1 shows an overview of some of the main accomplishments initially reported in the first two years (and some completed in the third year). We continued on the development of functional hybrid material platforms for high-speed optoelectronic devices (Figure 1(a)), plasmonic nonlinear photonic devices, especially second harmonic generation (Figures 1(b) and 1(c)), integrated photonic structures for comb generation based on dispersion engineering (Figure 1(d)), lateral heterostructures in 2D TMDCs for nonlinear and quantum photonic applications (Figure 1(e)), novel nonlinear devices through integration of PCMs with integrated photonic structures (Figure 1(f)), and a new integrated photonic/phononic platform for realization of SBS on chip. Each one of the resulting platforms can enable a series of devices/systems for nonlinear photonic applications with the potential to considerably improve the performance measures of the state-of-the-art structures.

Throughout this program, the potentials of several material systems for realization of nonlinear signal processing devices and systems were studied. In addition to forming hybrid material and device platforms using more conventional materials (e.g., Si and SiN), we have investigated the formation of new hybrid platforms using new materials such as lithium niobate ($LiNbO_3$) [1, 2] and SiC [3, 4]. On the device side, we have used new approaches for making devices in both the conventional and new material platforms to improve the nonlinear response. We also have developed fast and efficient nonlinear plasmonic devices including devices for efficient nonlinear SHG based on quasi-phase matching in plasmonic nanoantenna

arrays (Figure 1(b)) [5] and demonstration of ultra-fast hot-carrier-induced nonlinearity with exceptional nonlinear amplitude and phase responses [6, 7, 8].

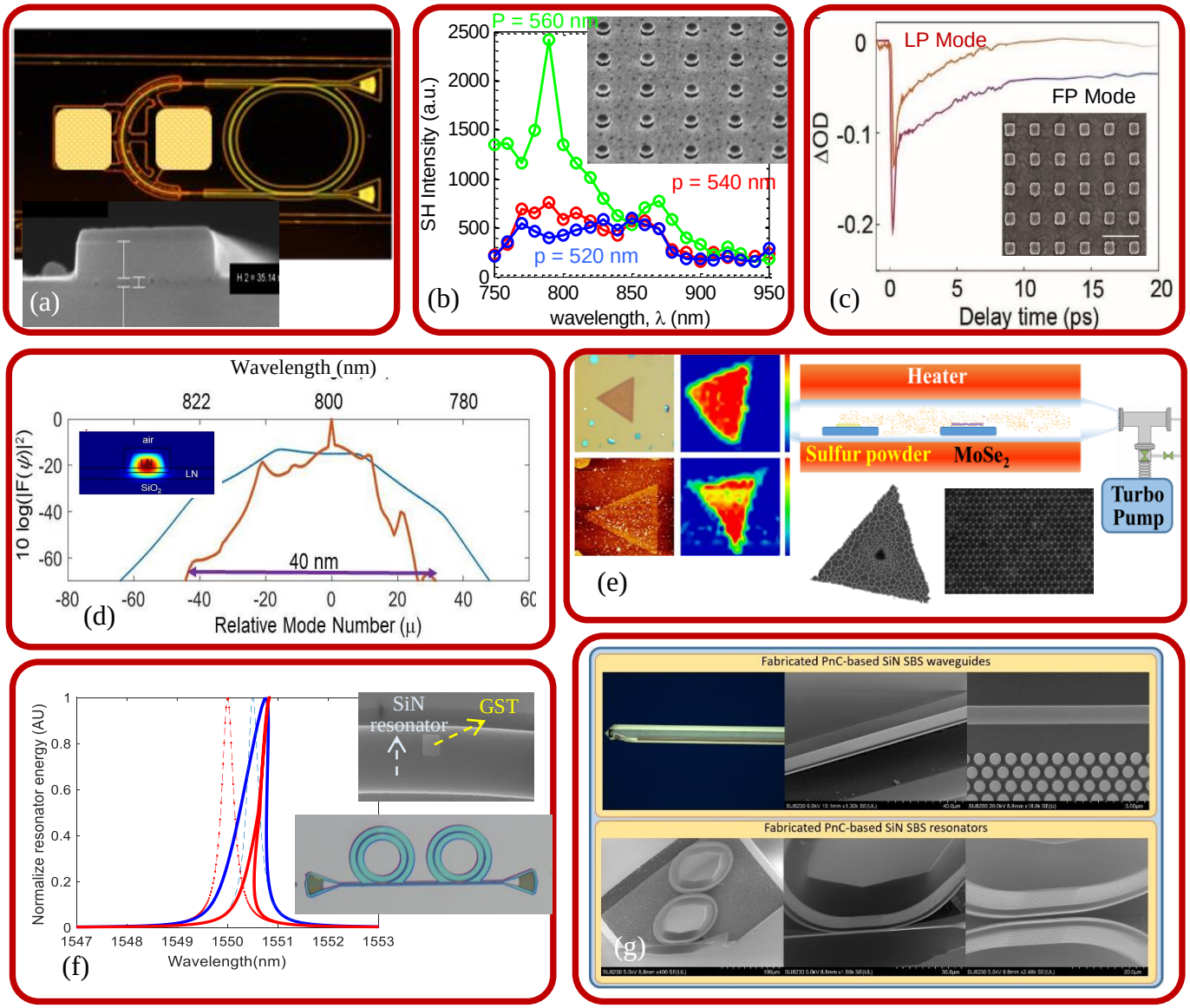

Figure 1, An overview of the research accomplishment supported by this program. (a) high-speed optoelectronic devices on hybrid material platforms, (b) Efficient phase-matched SHG in plasmonic nanoantenna structures, (c) ultra-fast hot-carrier nonlinearity in plasmonic nanostructures, (d) visible comb signals based on dispersion engineering in different material platforms (e.g., SiN, and $LiNbO_3$), (e) two-dimensional TMDC alloys and heterostructures, (e) nonlinear bi-stability in hybrid SiN and PCM nanoparticle structures, and (g) low-power SPS nonlinearity in waveguide and resonator-based SiN devices.

We have also continued our efforts on developing new mechanisms and material platforms for low-power nonlinear functionalities such as nonlinear signal generation and nonlinear switching including lateral heterostructures in 2D TMDCs (Figure 1(e)), low-power all-optical phase-transition in PCM nanoparticles (Figure (1(f)), and the low-threshold optomechanical nonlinearity in devices based on coupling between the resonant optical and acoustic modes in optomechanical structures as well as SBS in Si waveguides and resonators (Figure (1(g)). Our research in this areas has been reported in several recent publications [9,10,11,12].

II.B. Development of a high-quality SiC material and device platform for nonlinear photonic devices

SiC is a unique semiconductor material for optoelectronic applications as it provides a wide transparency window; strong thermal, mechanical, and optical properties; and relatively high second-order and third-order nonlinearities. The large indirect bandgap (> 2.2 eV) and high index of refraction (~ 2.6) of SiC allow to develop low-loss and compact integrated optoelectronic devices over a wide wavelength range from visible to mid-infrared (IR) [13]. In addition, the possibility of achieving low-loss and high quality-factor (Q) waveguides and resonators in SiC along with its relatively high third-order nonlinearity [14,15,16] enable to develop low-threshold nonlinear photonic devices for applications such as optical switching [17] and frequency comb generation [18]. Crystalline SiC has recently attracted attention for nonlinear and quantum optics applications, as it can harbor optically-active defects (i.e., vacancies) that can be employed as solid-state 'qubits' [19,20] for various nonlinear photonic (for all-optical signal processing) as well as spintronic and quantum information applications. Both optically-pumped [21] and electrically-pumped [22] SiC single-photon sources have been demonstrated at room temperature with high brightness and photo-stability.

To enable such nonlinear application of SiC, we have developed a high-quality 3C- SiC-on-insulator (SiCOI) integrated photonic material platform formed by wafer bonding of crystalline 3C-SiC to a silicon oxide (SiO_2)-on-Si substrate. We also have developed a unique process in the SiCOI platform for minimizing the effect of lattice mismatch during the growth of SiC on Si through polishing after bonding. This results in a high-quality SiCOI platform that enables microring resonators with record-high quality factors (Qs). The resulting SiCOI platform enables us to develop a wide range of nonlinear applications in integrated optics, including SHG, parametric down conversion, and nonlinear comb/soliton generation. At the same time, the semiconductor nature of SiC enables to realize tunable optoelectronic devices to achieve reconfigurable nonlinear photonic devices.

II.B.1. Development of a high-quality SiC material platform

Among three common polytypes of crystalline SiC, namely 4H, 6H and 3C, only cubic (3C) SiC can be epitaxially-grown on a Si substrate [23,24], which makes it compatible for integration with electronic devices. Several research groups have demonstrated integrated photonic devices (e.g., microcavities) on thin-film 3C-SiC [25,26,27,28,29,30,31,32,33,34], where the Si substrate is partially undercut to achieve photonic devices with light confinement in the SiC layer. However, such suspended devices suffer from low optical quality, low yield, and low reliability because of their fragile mechanical structures. The low optical quality is mainly due to the low optical quality (i.e., high-loss) of the SiC transition layer, which is caused by the high density of the defects due to the large Si/SiC lattice mismatch.

One solution for development of a high-quality 3C-SiC photonic material platform with mode confinement in the SiC film is to use a SiCOI structure. Previous efforts for forming high-quality SiCOI platforms have been focused on developing thin films from highly pure 6H/4H-SiC bulk wafers using the smart-cut technique [35, 36]. However, none of the previous attempts has resulted to a high-quality SiCOI platform.

In this program, we have used an optimized low-temperature hydrophilic bonding process [37,38] (developed through a previous AFOSR-funded project) to transfer an 800 nm-thick layer of 3C-SiC, epitaxially grown on a Si substrate, onto a 4 μm-thick thermally-grown SiO_2 layer on a Si substrate. The process can readily yield a high-quality SiCOI platform for integrated photonic devices without the need for undercutting the substrate or adopting high-loss processes. The SiC film is flipped through the bonding process, and the lower-quality SiC transition layer will be on the top of the transferred film in the SiCOI platform, and it is removed by chemical mechanical polishing (CMP). After polishing only 100 nm from the top of the SiC film on the SiCOI platform, we achieve a factor three reduction in the surface roughness

of the 3C-SiC film, me asured using atomic force microscopy (AFM). This process enables us to achieve low-loss waveguides (loss <1.7 dB/cm) and high Q resonators (Q>242,000) [39], which are the best reported results for SiC devices to-date.

Figure 2 shows the fabrication process flow of our SiCOI platform based on transferring of a thin 3C-SiC layer from the Si substrate onto a low-refractive index SiO_2 (thickness: 4 µm) on a Si substrate. A thin layer of 3C-SiC is epitaxially grown on a Si substrate (NOVASiC SA) and then is polished using chemical-mechanical polishing (CMP) to reduce the surface roughness and thinned-down the SiC layer thickness to the desired thickness (e.g., 800 nm) (Fig. 2(b)). A 30 nm-thick SiO_2 layer is deposited on the SiC film after CMP using atomic layer deposition (ALD). The SiC wafer is then bonded to a Si wafer with 4µm of thermal-oxide through a wafer-scale low-temperature (300 °C) hydrophilic bonding process (Fig. 2 (f)). Finally, the Si handle layer of the SiC wafer is removed using a combination of Bosch dry-etching process and potassium hydroxide (KOH) wet etching (Fig. 2 (g)). Figure 2 inset shows a photo of the developed 2 inch by 2 inch SiCOI platform with nearly 100% yield.

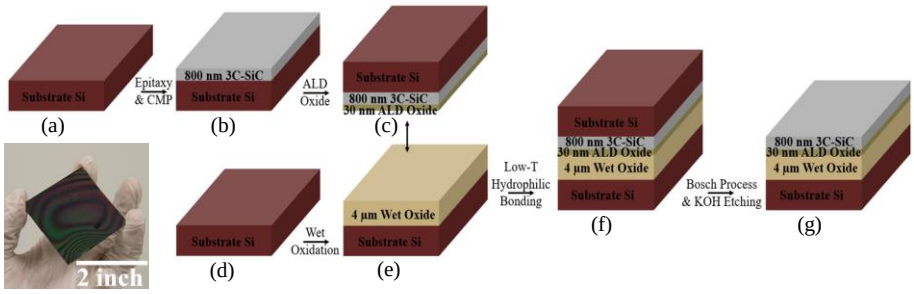

Figure 2, Fabrication process flow of the SiCOI material platform. (a) Piece #1, a prime Si wafer. (b) Epitaxial growth of 3C-SiC with top surface smoothened by CMP, leaving a 3C-SiC film with an average thickness of 800 nm (thickness variation ~ 100 nm). (c) Deposition of a 30 nm SiO_2 layer using ALD. (d) Piece #2, a prime Si wafer. (e) Wet oxidation to grow 4 µm of thermal SiO_2. (f) Piece #1 and piece #2 are bonded using a low-temperature hydrophilic bonding process. (g) Removal of the Si handle layer using Bosch process and KOH wet etching. Inset: A photo of the bonded SiCOI piece.

Figure 3 (a) shows the cross-section of a SiC-on-Si sample before the bonding process. We can clearly observe large defects (voids) at the SiC/Si interface. These interfacial defects are formed at the transition layer during the SiC layer growth (epitaxy) due to the large lattice and thermal-expansion-coefficient mismatches of Si and SiC, which in turn, result in a low-optical-quality deposited film at the first few 100's of nm of the grown SiC film (i.e., transition layer) [40]. As it can be seen from the cross-sectional SEM images, the SiC layer after the initial after-growth CMP has an average thickness of 800 nm (thickness variation ~ 100 nm). Figure 3 (b) shows the cross-section SEM image of a SiCOI sample, where the SiC layer is on the top of the buried oxide (BOX) layer (similar to a commercial silicon-on-insulator (SOI) wafer, with SiC instead of Si as the device layer). While the thickness of the SiC layer has not changed in this process, the SiC film is flipped upside down, and the SiC transition layer is now on the top of the SiCOI platform.

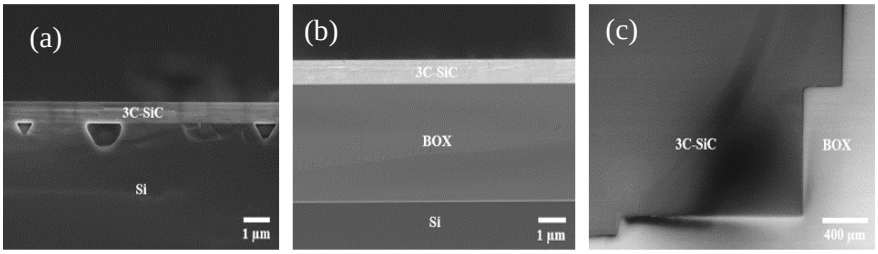

Figure 3, (a) Cross-sectional SEM image of the original 3C-SiC-on-Si sample. The average thickness of the SiC film is 800 nm. (b) Cross-sectional SEM image of the SiCOI sample. The average thickness of the SiC film maintains as 800 nm. The thickness of the BOX layer is 4 µm. (c) Top view SEM image of the broken edges of the SiCOI sample along the SiC crystal directions.

To monitor the quality of the SiC/Si transition layer, we conduct transmission electron microscopy (TEM) on a SiCOI lamella etched and transferred onto the TEM grid by focused ion beam (FIB) incorporated with a micro-manipulator and SEM. Figure 4 (a) shows the zoomed-out view of the SiCOI lamella. It shows the cross-sectional structure of the SiCOI sample. The platinum (Pt) layer on top of SiC is to protect its surface from being exposed to the ion beam. The line-shape patterns shown in the region where SiC exists stem from the diffraction of electrons due to the defects of the SiC lattice. It is clearly shown that the density of the diffraction pattern becomes much higher when it approaches the top of the SiCOI lamella where the transition layer sits. Figure 4 (b) shows a zoomed-in view of this transition layer at the atomic scale; it clearly shows a high density of defects as well as stacking faults in the SiC crystal. The transition layer has high-density defects, which will cause scattering and absorption of light inside the material. However, when it comes to the other side of the SiC film (i.e., the bottom of the SiC layer in the SiCOI lamella), as shown in Figure 4(c), SiC atoms are uniformly stacked. We also perform AFM measurement on the grown SiC at Si/SiC interface (now on the top of the SiCOI platform) to analyze the root-mean-squared (RMS) roughness (σ) of the device top surface. We measure σ ~ 1.33 Å with a range from -4.538 Å to 5.152 Å, which is close to the surface roughness of ultra-low-loss Si3N4 [41]. However, the 2D AFM scan of the top layer of the SiCOI sample (which is the SiC/ Si interface layer) shows a roughness of σ = 7.25 Å with a range from -2.5 nm to 3.5 nm, which is 5-7 times higher than that of the top layer of the original sample. This large roughness mainly comes from lattice dislocations at the SiC/Si interfacial layer.

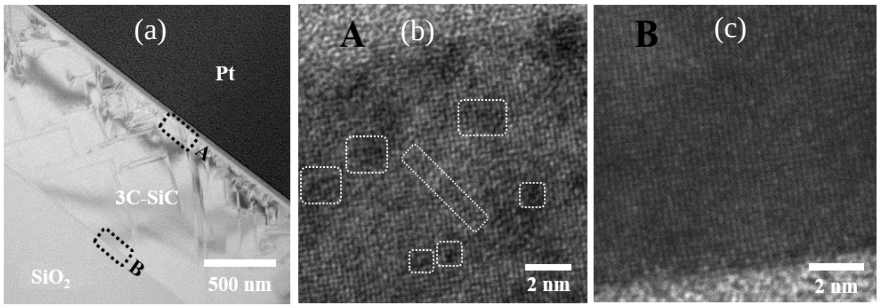

Figure 4, Zoomed-out TEM image of the SiCOI lamella. The line-shape patterns shown in the region where SiC exists are from the diffraction of electrons due to the defects of the SiC lattice. (b) Zoomed-in TEM image of the top surface of a SiCOI lamella (region A in (a), also known as the transition layer) where there is a high density of defects. Some of the regions with defects are indicated by white color. (c) Zoomed-in TEM image of the bottom layer of the SiCOI lamella (region B in (a)) where there is a low density of defects in SiC.

To reduce the scattering losses from the Si/SiC interfacial layer, we use CMP (Entrepix, Inc) to reduce the roughness of the top layer of the SiCOI sample. The 2D AFM scan after the final CMP shows that the σ has decreased from 7.25 Å to 2.47 Å with range from -8.824 Å to 9.963 Å (reduced by a factor of three).

To assess the optical quality of the developed SiCOI platform after and before the CMP step, we fabricated different microresonator devices (designed for C-band telecom wavelength range, i.e. ~1550nm) on the SiCOI platform before and after the last CMP process. We use alumina (Al_2O_3) as a hard mask patterned by electron beam lithography (EBL) with negative resist flowable oxide (FOX, Dow Corning) and SiC dry etching using reactive-ion etching (RIE) with a fluorine-based plasma chemistry (CHF_3/O_2). Our developed process is simpler, and provides good etching selectivity and better side-wall roughness's as compared to the previously reported approaches based on using metal masks [42, 43].

Figure 5(a) shows example SEM of the fabricated devices on the SiCOI platform. Figures 5(b, c) show an example of the measured resonance spectru m of a waveguide-coupled resonator on the SICOI platform after and before CMP process. The comparison of the quality factor of the devices before and after CMP on our SiCOI platform shows an improvement in the intrinsic Qs of similar resonators on the SiCOI after the polishing to 126k (20 µm-radius micro-donut) as compared to 42k before CMP process (~three times improvement) [44]. This is in agreement with our AFM measurement for surface roughness on the SiC. We

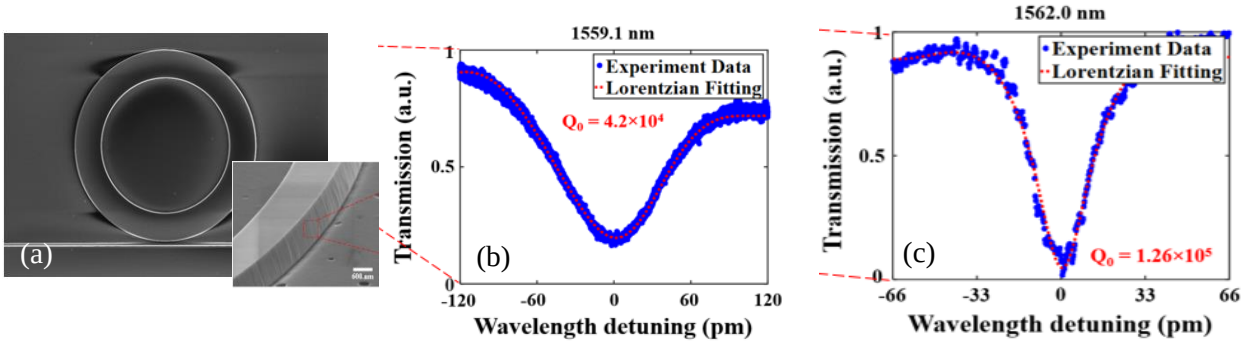

Figure 5, (a) Top view SEM image of a 20 µm-radius micro-donut resonator-waveguide coupled region. The thickness of the device is 500 nm. (b) Transmission spectrum of a 20 µm-radius micro-donut resonator under TE polarization near 1550 nm wavelength. (c) Normalized transmission spectrum of the resonant mode at 1562.0 nm marked in (b), with experimental data and Lorentzian fitting shown in blue and red, respectively. The mode is near-critically coupled with an intrinsic Q of about 126,000.

have also achieved Qs of 242k for microring resonators on the same platform.

Furthermore, we demonstrated high-Q SiC resonators at IR and visible wavelengths by polishing down the SiC layer (~ 800 nm) on our SiCOI to 500 nm and 250 nm, respectively. We achieved a further reduction of surface roughness to 1.4 Å (compared to 2.5 Å), by an additional step of CMP, which is nearly the same as that of the original polished SiC surface on top of a 3C-SiC-on-Si sample. We also demonstrated a

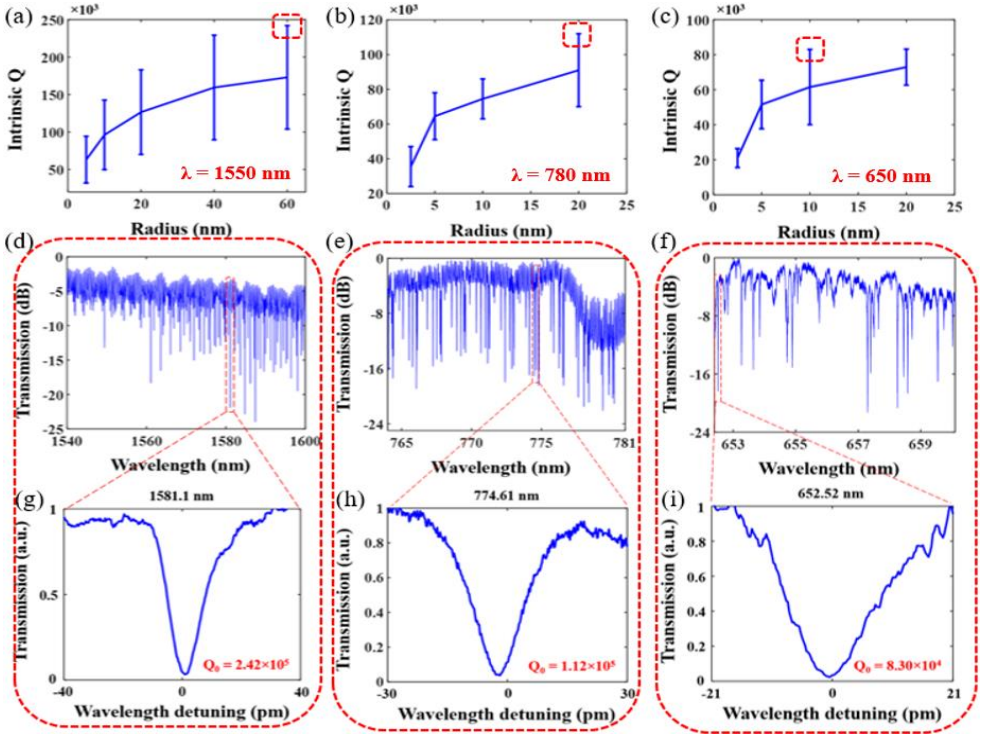

Figure 6, The measured intrinsic Qs versus the outer radius of the microdisk resonators at (a) 1550 nm, (b) 780 nm, and (c) 650 nm wavelengths. Transmission spectrum of (d) 60-µm radius microdisk resonator at 1550 nm, (e) 20-µm radius microdisk resonator at 780 nm, and (f) 10-µm radius microdisk resonator at 650 nm. Normalized transmission spectrum of the resonant mode (g) at 1581.1 nm marked in (d) with an intrinsic Q of 242,000, (h) at 774.61 nm marked in (e) with an intrinsic Q of 112,000, and (i) at 652.52 nm marked in (f) with an intrinsic Q of 83,000.

series of microdisk resonators working at around 1550 nm on the 500-nm thick SiC film as well as resonators working at around 780 nm and 650 nm on the 250 nm-thick SiC film. We demonstrated record-high Qs of 242,000 at 1550 nm, 112,000 at 780 nm, and 83,000 at 650 nm [45] (Figure 6). These results prove the unique capabilities of our SiCOI platform in form high-Q SiC resonators at a broad wavelength range. This platform sets the stage for the development of high quality factor SiC devices for nonlinear applications at both visible and IR wavelengths. We believe that the Q of the resonators on the SiCOI platform can be further improved by starting from a thicker SiC on Si film and removing more of the transition SiC layer (e.g. 500 nm as compared to 100 nm in this work) and by some adjustment in our etching process.

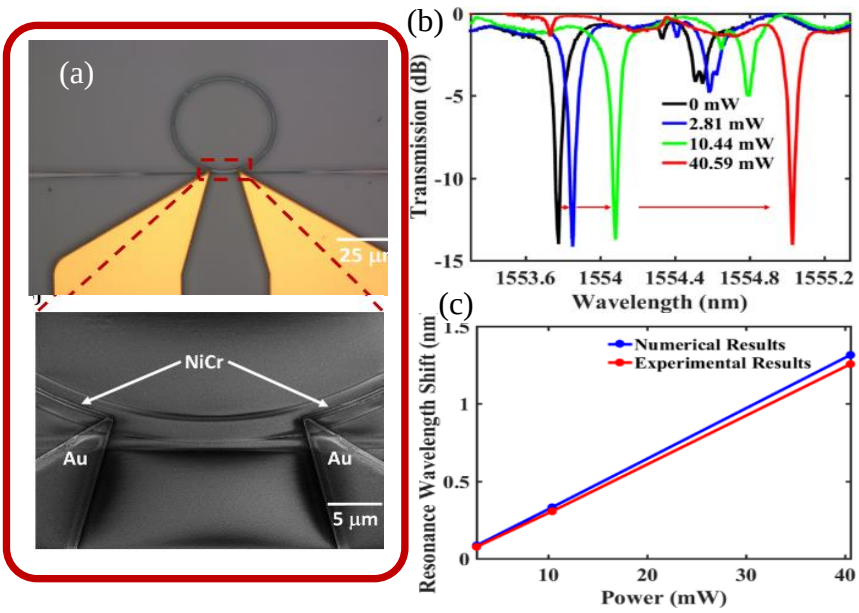

Figure 7, (a) The optical micrograph of microring resonator with the integration of microheater. Insets are the zoomed-in SEM image of the coupling region of the device and its transmission spectra showing an intrinsic Q of 88,000. (b) The experimentally measured transmission spectra of the microring resonator and (c) the numerical and experimental results of the resonance wavelength shift with different power dissipations.

We also demonstrated thermally-reconfigurable high-Q SiC microring resonators with integrated microheaters on a 3C-SiCOI platform. This platform offers an easy and reliable way for integration with electronic devices as well as great potentials for diverse integrated optics applications. We extracted a thermo-optic coefficient of around 2.67×10^{-5} /K for 3C-SiC from wavelength shift of a resonator heated by a hot plate. Finally, we fabricateed a 40 μm-radius microring resonator with intrinsic Q of 88,000 at infrared wavelengths (~1550 nm) after integrated with NiCr microheater. By applying current through the microheater, a resonance shift of 30 pm/mW was achieved in the microrings, corresponding to ~50 mW per π phase shift [46] (Figure 7). We have also designed more efficient and fast thermally reconfigured SiC structures, which will be tested soon, that take advantage of the high thermal conductivity of SiC to achieve very fast reconfiguration times (< 100's ns) and considerably lower power consumptions, by directly integrating the heater on the SiC devices. Along with the thermally tunable SiC devices, we also have designed SiC reconfigurable devices based on carrier accumulation for much ultra-fast and low- power reconfigurable devices, in expense of slightly higher loss, and lower tuning dynamic range.

II.C. Heterostructures in 2D TMDCs as a promising platform for nonlinear photonic devices

As it was explained in the last annual report, 2D TMDCs provide specific advantages that make them a great alternative for demonstration of fast and efficient nonlinear photonic devices. The fast carrier dynamics of TMDCs along with their strong interaction with light and their high sensitivity of their effective refractive index to modulation of carrier density enable efficient all-optical nonlinear processing based on both second-order and third–order nonlinearities. Our focus on development of nonlinear photonic structures based on 2D MDCs has been based on developing in-plane (i.e., lateral) 2D TDMC heterostructures (e.g. lateral quantum dots and quantum wells), which we expect to greatly enhance the nonlinear optical properties of the 2D TMDCs. We have developed a technique for selective area 2D TMDC composition modulation, which enables us to locally engineer the 2D TMDC material band structures and

design heterostructures with the desired profile. In the last annual report, we reported our achievement on development of ternary 2D TMDCs (MS_xSe_{2-x}) alloys with desired composition through the sulfurization of selenide-based TMDCs (i.e., MSe_2) as well as our effort on development of heterostructures based on lithography-defined (E-beam lithography) selective masking of the TMDCs during the sulfurization process. We also reported the issue of the crack formation in the converted (i.e., composition modulated) TMDC caused by the conversion-induced strain. Following this effort, we have carefully studied the fundamental causes of the crack formation and found the relation of the defects in the initial TMDC (here $MoSe_2$) monolayers on the crack-formation process. Furthermore, we used an arsenal of different characterization techniques (e.g., Raman, Low-temperature photoluminescence (PL), and scanning transmission-electron microscopy (STEM)) along with theoretical studies based on density function theory (DFT) to study the conversion process. By studying the difference between the conversion process in the CVD (chemical vapor deposition)-deposited and exfoliated monolayers $MoSe_2$ samples (with different growth condition), we found that the defects play an important role in the conversion process. This not only provides a better understanding of the process for the development of the 2D TMDC heterostructures, but enables us to use defect engineering as a tool to achieve a better control over the composition and the geometry of the designed TMDC heterostructure devices.

II.C.1. Overview of the TMDC alloying and heterostructure development

Alloying of TMDCs has long served as a key technique for tuning their optoelectronic properties [47, 48]. Indeed, in ternary TMD alloys (i.e., $MX'_{2x}X_{2(1-x)}$ or $M'_xM_{1-x}X_2$; M, M': transition metals and X, X': chalcogens), tuning the composition ratio (i.e., x) enables customizing the bandgap of 2D materials, offering specifications that binary crystals (i.e., MX_2) fail to provide. In addition to the rudimentary bandgap tuning, alloying methods based on the post-growth composition modulation of binary crystals have found unique applications in the synthesis of lateral heterostructures with arbitrary shapes and dimensions [49, 50].

Our two-step alloying approach employs a standard CVD method for synthesis of monolayer TMDC composed of metal M and chalcogen X (e.g., $MoSe_2$ crystals) (first step) followed by a high temperature exposure to a different chalcogen (X') to incorporate foreign atoms (e.g., S) into the host lattice of the MX_2. The chalcogen substitution (i.e., sulfurization or selenization) step is done using a high-temperature annealing process under a chalcogen vapor ambient in a dedicated furnace [51]. The degree of the sulfurization can be controlled by adjusting sulfurization process temperature and time to achieve alloys with different stoichiometry (Figure 8(a)).

The SEM inspection of several independently converted samples consistently confirms that more than ~ 90 % of the converted MoS_2 monolayer crystals are entirely cracked (Figure 8(b)). The formation of the cracks can

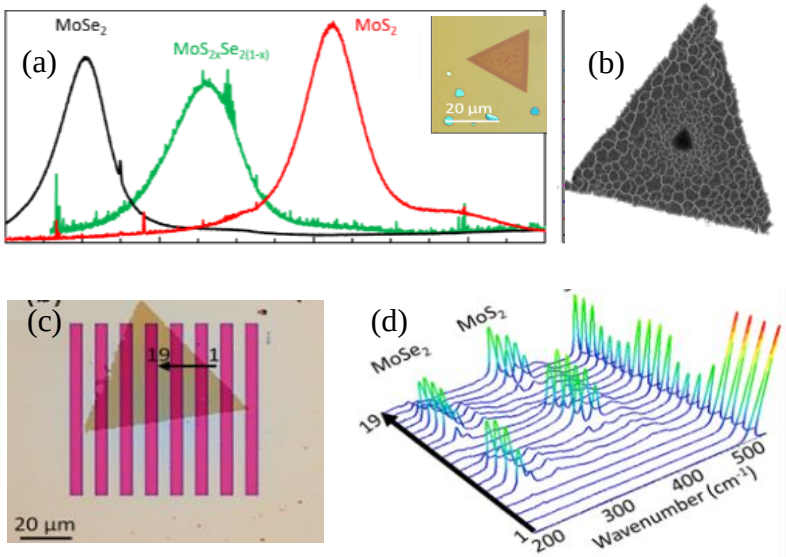

Figure 8, (a) (b) PL spectroscopy representing continuous tuning of the light emission energy (or the bandgap) between individual emission lines corresponding to pristine MoS_2 and $MoSe_2$. Similar tuning effect can be observed via Raman spectroscopy. (b) Crack formation in converted MoS_2 monolayer crystals (SEM of an entirely cracked flake). (c,d) Experimental demonstration of the lithography-assisted approach for fabrication of lateral heterostructures (e.g., MoS_2-$MoSe_2$); (c) optical image of the structure and (d) Raman measurements across the line shown in (c).

be attributed to the post-alloying strain caused by lattice constant mismatch between MoS_2 and $MoSe_2$ and the thermal-expansion (in the high temperature conversion process) (leading to a total stress of 4% to 5%) along with the reduces critical strain of MoS_2 (down from 11% to less than 4%) by the pre-existing defects/cracks in the initial 2D material (and those generated during the conversation process). The calculations based on Griffith method [52] show that defect sizes in the range of 1 nm (corresponding to a few atom vacancies) can lead to cracks with strains as low as 4%. Our initial TEM study of the $MoSe_2$ samples show that the initial CVD $MoSe_2$ has a relatively high density of such defects. In the next section, we will explain how this challenge can be addressed.

We have also developed an alternative lithography-assisted approach for the realization of lateral heterostructures based on selective compositions modulation. In this approach, using standard lithography techniques combined with deposition methods (e.g., e-beam evaporation), parts of a pre-grown 2D TMDC film are protected with a mask and unprotected regions are selectively converted into a different 2D material (using the indirect alloying method explained in previous sections). Our experimental results demonstrate the possibility of achieving lateral $MoSe_2/MoS_2$ HSs based on selective area composition modulation of a pre-grown $MoSe_2$ crystal (Figure 8(c, d)). The proposed lithography-based approach enables to deterministically form lateral heterostructures with intended lateral dimensions and position. These features are essential for integration of 2D heterostructures in hybrid optoelectronic devices using mainstream CMOS fabrication processes. Moreover, the application of nanolithography techniques (e.g., EBL) enables to fabricate quantum-confined lateral heterostructures with fine feature sizes (< 10 nm).

II.C.2. Fundamental study of the role of the defects in the development of 2D TMDC alloys and heterostructures

Despite the diverse extent of current studies, the role of native defects in the alloying of monolayer TMDCs has remained largely unexplored. In the post-growth alloying approach, the presence of native defects in the starting host crystal may affect the details of the alloying process as well as the ultimate properties of ternary crystals synthesized via the post-growth alloying approach. Since we synthesize $MoS_{2x}Se_{2(1-x)}$ films using the post-growth alloying method, the quality of starting $MoSe_2$ films has a significant influence on the obtained properties of alloys as well as on required sulfurization parameters.

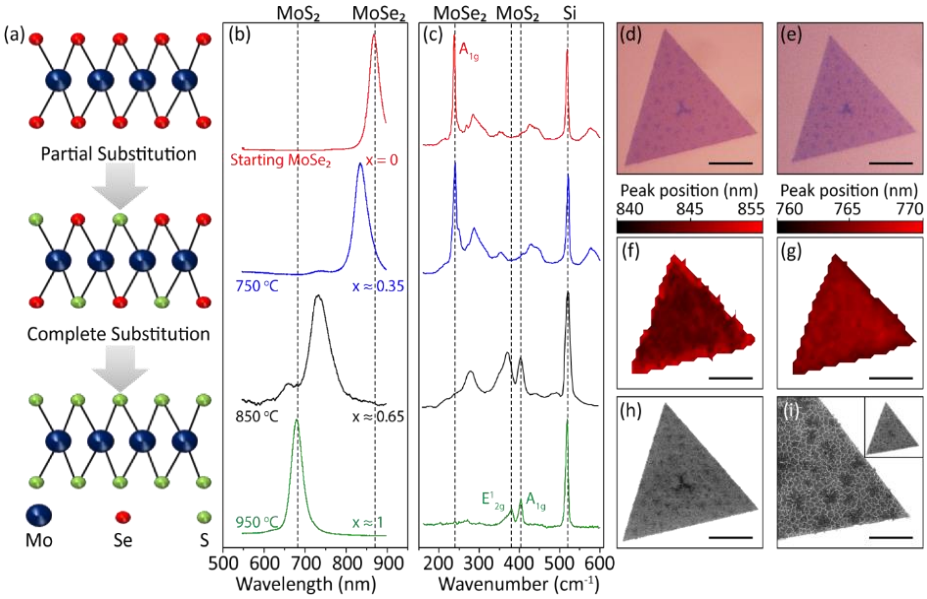

Figure 9, Synthesis of 2D ternary alloys via the chalcogen substitution. (a) Schematic representation of the alloying process. (b, c) Representative PL and Raman spectra, respectively, acquired from CVD-grown $MoSe_2$ monolayers sulfurized at various temperatures for 20 mins. Composition ratios (i.e., x) are marked on the PL spectra in (b). (d, e) The optical-microscope images and (f, g) PL maps of a representative monolayer film before and after sulfurization (850 °C, 20 mins), respectively. (h) The SEM image of the $MoSe_2$ film before sulfurization. (i) The SEM image taken from the bottom-right corner of the triangle after the sulfurization.

To study the effect of the defects on the conversion process, we perform our sulfurization process on both

"CVD-grown" and "exfoliated" $MoSe_2$ monolayers and compare the properties of obtained alloys. We expect that the difference between the defects type, density, and size in CVD-grown and exfoliated $MoSe_2$ monolayers should guide us to a better understanding of the sulfurization process.

The PL spectroscopy performed on CVD-grown $MoSe_2$ samples sulfurized at different temperatures (Figure 9(b)) demonstrates that sulfurization at 950 ^oC for 20 mins leads to the complete replacement of Se atoms by S atoms, converting the starting $MoSe_2$ crystal (x = 0, PL peak ≈ 870 nm) into a MoS_2 crystal (x = 1, PL peak ≈ 680 nm). Accordingly, sulfurization at lower temperatures (ranging from 700 ^oC to 950 ^oC) leads to the partial substitution of chalcogen atoms (i.e., $0 < x < 1$) and the synthesis of ternary alloys. We also drew a similar conclusion from Raman spectroscopy (Figure 9(c)), where, the A_{1g} Raman mode of the starting $MoSe_2$ monolayer at 240 cm^{-1} gradually disappears, and the E^1_{2g} and A_{1g} modes of the MoS_2 monolayer at 381 cm^{-1} and 401 cm^{-1} emerge upon increasing the sulfurization temperature. We used the PL spectroscopy to estimate the composition ratio of $MoS_{2x}Se_{2(1-x)}$ alloys synthesized at various sulfurization conditions (labeled in Figure 9(b)). [30] In addition, we employed the PL mapping before and after the sulfurization of CVD-grown $MoSe_2$ monolayers (Figures 9(d)-(g)) to explore the spatial uniformity of the chalcogen replacement across the plane of the 2D material. As Figure 9(g) shows, for a sample sulfurized at 850 ^oC for 20 minutes, the PL map displays a relatively uniform PL emission profile (765 ± 5 nm, x ≈ 0.45 ± 0.04), suggesting that the chalcogen substitution takes place uniformly across the entire plane of the 2D material. Our experiments showed that such a notable spatial uniformity is also achievable in $MoS_{2x}Se_{2(1-x)}$ alloys with other values of x.

Figures 10(a-f) display the optical images, PL maps, and SEM images of an exfoliated $MoSe_2$ film before (top row) and after (bottom row) sulfurization at 950 ^oC for 20 minutes. The representative PL and Raman spectra of the sample are also shown in Figures 10(g) and 10(h), respectively. In these figures, the blue-shift of the PL peak as well as the emergence of two new Raman peaks (around 400 cm^{-1}) prove the successful incorporation of S atoms into the lattice of exfoliated $MoSe_2$ films. The $MoS_{2x}Se_{2(1-x)}$ alloys synthesized from exfoliated $MoSe_2$ crystals have two distinguishable differences compared to those synthesized from CVD-grown $MoSe_2$ films. First, unlike CVD-grown samples, the sulfurization of

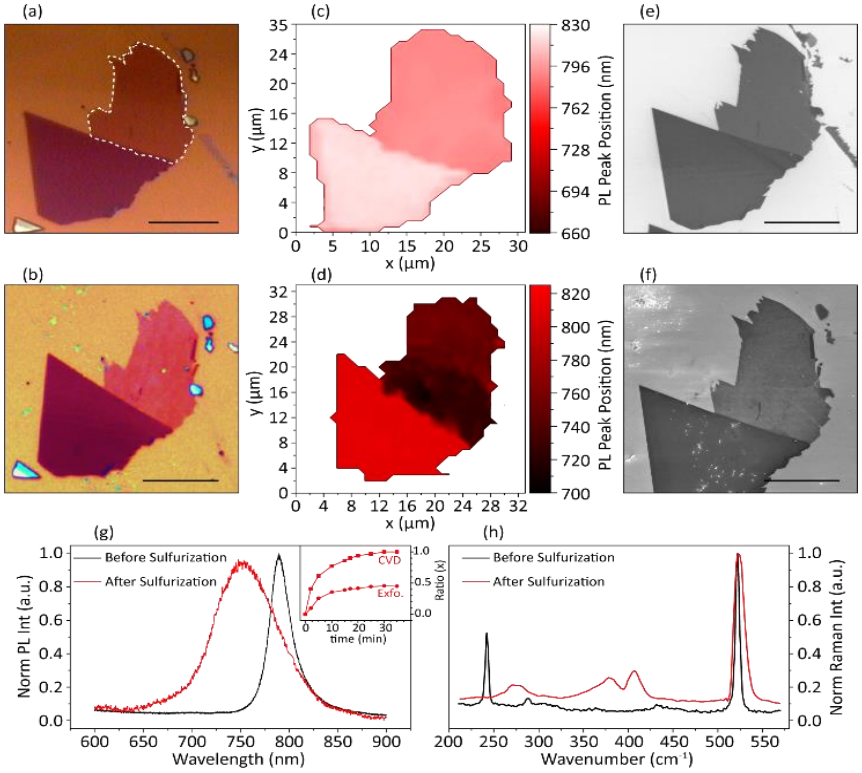

Figure 10, Alloying of exfoliated $MoSe_2$. (a, b) Optical images of an exfoliated $MoSe_2$, (c, d) The PL mapping of the sample, (e, f), the SEM images of the film, and (g, h) Representative normalized PL and Raman spectra of the sample, before and after the sulfurization process (950 ^oC, 20 minutes). The dashed line in panel (a) outlines the monolayer region. The alloying process does not generate cracks in the exfoliated crystal. The inset of panel (g) displays x values obtained at different sulfurization times (temperature was fixed at 950 ^oC). The chalcogen substitution ratio in exfoliated samples saturates at x ≈ 0.45 after 20 minutes of sulfurization, while that in CVD-grown samples saturates at x = 1 (complete saturation). Scale bars represent 10 μm.

exfoliated $MoSe_2$ films yields alloys with seamless structures without any cracks (Figure 10(f)). Using complementary experiments, we confirmed that the absence of cracks in alloys synthesized from exfoliated $MoSe_2$ films is independent of the sulfurization temperature and the composition ratio. Second, the chalcogen exchange in exfoliated $MoSe_2$ monolayers is more challenging than that in CVD-grown ones. For instance, sulfurization at 950 ^oC for 20 minutes enables near-complete chalcogen replacement in CVD-grown $MoSe_2$ monolayers (Figure 9), while an identical sulfurization condition leads to only 35-50 % chalcogen replacement in exfoliated monolayer crystals (Figure 10). Thus, to excel further chalcogen substitution in exfoliated $MoSe_2$ films, the sulfurization process needs to be performed at temperatures above 950 ^oC, which is out of the reach of our experimental setup. Alternatively, we extended the sulfurization time to allow for more chalcogen substitution. However, as the inset of Figure 10(g) shows, the chalcogen substitution in exfoliated films saturates at $x \approx 0.45$ after ~ 30 minutes of sulfurization at 950 ^oC, which indicates that a temperature-driven mechanism governs the extent of the chalcogen replacement. Interestingly, under identical sulfurization conditions, a similar saturation effect occurs in CVD-grown samples, but the saturation point is at a significantly larger value of $x \approx 1$ (the inset of Figure 10(g)). Therefore, we conclude that replacing chalcogen atoms in exfoliated $MoSe_2$ monolayers is less efficient than that in CVD-grown samples. Considering consistent sulfurization conditions used for CVD-grown and exfoliated $MoSe_2$ monolayers, we infer that the characteristic material properties of the host $MoSe_2$ film play the primary role in the obtained attributes of the as-synthesized $MoS_{2x}Se_{2(1-x)}$ alloys.

Our AFM analyses of CVD-grown and exfoliated $MoSe_2$ films also revealed that, unlike exfoliated films, CVD-grown $MoSe_2$ films contain large-scale defects with sizes typically ranging from several nanometers (nm) to ~ 100 nm. Such a span of the defect size can cause cracking under alloying-induced strain values as small as ~0.8%, corresponding to $MoS_{2x}Se_{2(1-x)}$ alloys with composition ratios as small as $x \approx 0.2$. Therefore, we conclude that the presence of large-scale defects in the form of pre-existing cracks in CVD-grown $MoSe_2$ films contributes to the formation of cracked alloys and the absence of such defects in exfoliated crystals yields seamless alloys without any cracks. A recent study [53] shows that the Griffith method overestimates the strength of defective 2D materials especially when the defect size is smaller than 10 nm. Therefore, the range of defect sizes that we measured in CVD-grown $MoSe_2$ films can generate cracks in alloys with x values even smaller than 0.2.

In addition to large-scale defects, TMD crystals are known to host point defects of various types and densities [54,55,56,57]. Such point defects may serve as atomic-scale sites from which the S atoms incorporate into the lattice of $MoSe_2$ crystals, hence, promoting the chalcogen replacement during the sulfurization process. Therefore, probing point defects in the starting $MoSe_2$ films can shed light on the atomic-scale details of the alloying process and help explaining the different chalcogen-substitution behaviors we observed in CVD-grown and exfoliated samples (i.e., the inset of Figure 10(g)). Point defects can be robustly probed via monitoring the optical states that they induce within the bandgap of an otherwise perfect semiconductor [58,59]. However, because of the strong thermal broadening, such mid-gap optical states should be monitored at low temperatures. Therefore, to explore the presence of pre-existing native point defects, we carried out low-temperature (~ 4K) PL spectroscopy on exfoliated and CVD-grown $MoSe_2$ monolayers (Figure 11), and, via analyzing defect bands, we explored the role of native point defects in the post-growth alloying of $MoSe_2$ films.

The low-temperature PL spectra of exfoliated $MoSe_2$ films (Figure 11(a)) display two spectrally-symmetric emission peaks at ~ 745 nm and ~ 760 nm associated with neutral excitons (X^o) and charged excitons (i.e., trions (T)), respectively. We measured a bonding-energy difference of ~ 30 meV between Xo and T that agrees with previous reports [60]. In addition to X^o and T emissions, we identified a spectrally-asymmetric emission line at longer wavelengths that can be deconvoluted into multiple Gaussian lineshapes with emission energies ~ 0.15-0.2 eV below the X^o energy. We attribute these emission bands to the

radiative recombination of excitons trapped by defect states in exfoliated $MoSe_2$ monolayers, and we refer to them as defect-trapped excitonic emissions (X^d). This matches previous experimental observations and theoretical predictions based on DFT calculations, which suggest the formation of defect-induced mid-gap states ~ 0.2-0.3 eV away from the edge of the conduction/valance band in $MoSe_2$ films [61]. We further verified the nature of the X^d emission via monitoring its integrated PL intensity as the power of the excitation laser changes (Figure 11(b)). Since the X^d emission stems from defect-mediated radiative recombinations, its emission intensity saturates at high excitation powers after defect states are fully populated with free excitons. Our experiments meet this expectation as the emission intensity of X^d displays a sub-linear dependence on the excitation power, manifesting the saturation of the PL intensity at high excitation powers. In contrast, X^o and T emission bands follow linear trends with no sign of saturation within the measured excitation power range.

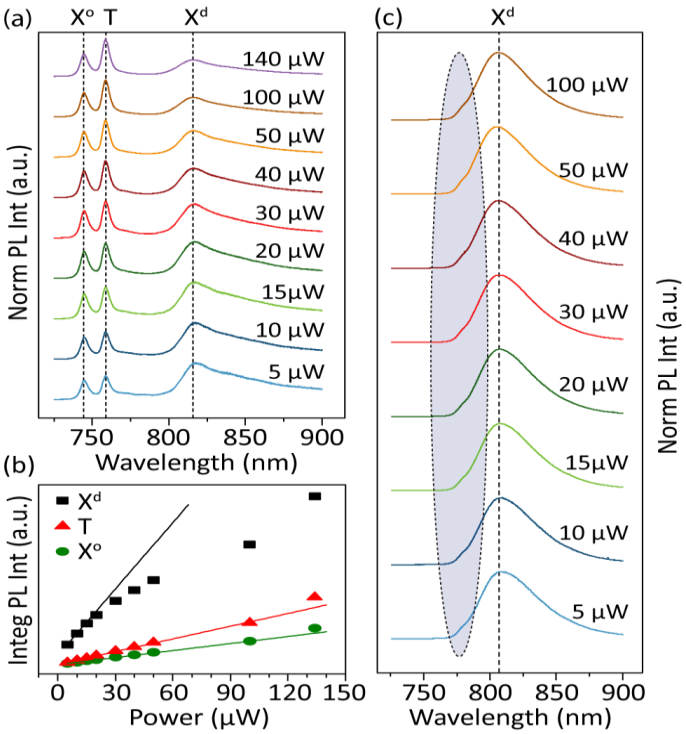

Figure 11, Low-temperature (~ 4K) PL spectroscopy of defects in $MoSe_2$ monolayers. (a) PL spectra obtained from a representative exfoliated $MoSe_2$ sample. Excitation powers are marked on the spectra. Three emission lines marked on the spectra associate with neutral excitons (X^o), trions (T), and defect-trapped excitons (X^d). (b) The integrated PL intensities of X^o and T emissions demonstrate linear dependence on the excitation power, while a sub-linear trend governs the behavior of the X^d emission. (c) PL spectra obtained from a representative CVD-grown $MoSe_2$ sample. Excitation powers are marked on the spectra. The defect-assisted emission dominates the PL spectra of CVD-grown samples, and X^o and T emissions only appear as weak peaks on the shoulder of the X^d emission. The shaded oval region highlights the approximate locations of X^o and T peaks.

In comparison to exfoliated $MoSe_2$ crystals, CVD-grown crystals display strikingly different low-temperature PL spectra (Figure 11(c)). In fact, in CVD-grown samples, the defect-mediated emission (i.e., X^d) overwhelms the entire PL spectrum, and the emissions of free excitons/trions only appear as weak peaks on the short-wavelength shoulder of the broad X^d band, as highlighted by the shaded oval in Figure 11(c). In addition, within our accessible range of the excitation power, we did not observe any saturation in the emission intensity at the X^d band of CVD-grown films. These collective observations suggest that the density of point defects in CVD-grown $MoSe_2$ monolayers is significantly larger than that in exfoliated $MoSe_2$ monolayers.

To further study native point defects, we performed scanning transmission-electron microscopy (STEM) imaging on CVD-grown (Figure 12(a)) and exfoliated (Figure 12(b)) $MoSe_2$ monolayers. To identify defect types and to estimate the areal density of defects, we relied on the image-intensity variation at atomic sites (Figure 12(c)). In STEM, the image intensity is proportional to the atomic number (Z) as well as the number atoms occupying a site. Thus, the chalcogen sites with two Se atoms (Z = 34) appear slightly brighter than the metal sites with only one Mo atom (Z = 42). Accordingly, using intensity mapping across atomic lines (e.g., Figure 12(c)), we first distinguish the chalcogen sub-lattice from the metal sublattice. Therefore, lattice distortions or defects can be immediately identified through deviation from the benchmark intensity profile shown in the left panel of Figure 12(c). For instance, as Figure 12(c) (middle panel) represents, the intensity at a single Se-vacancy (V_{Se}) with only one Se atom is approximately half of

the intensity at a chalcogen site that is occupied by two Se atoms, and the intensity at a double-Se vacancy (V_{2Se}) drops to the background level because there is no Se atom at such atomic sites. Using this criterion, we analyzed STEM images and concluded that the V_{Se} vacancy is the dominant defect type in both CVD-grown and exfoliated $MoSe_2$ films. In addition to V_{Se} vacancies, CVD-grown $MoSe_2$ films also host V_{2Se} vacancies at a relatively lower density. We did not observe other types of point defects or any extended defects in either $MoSe_2$ samples.

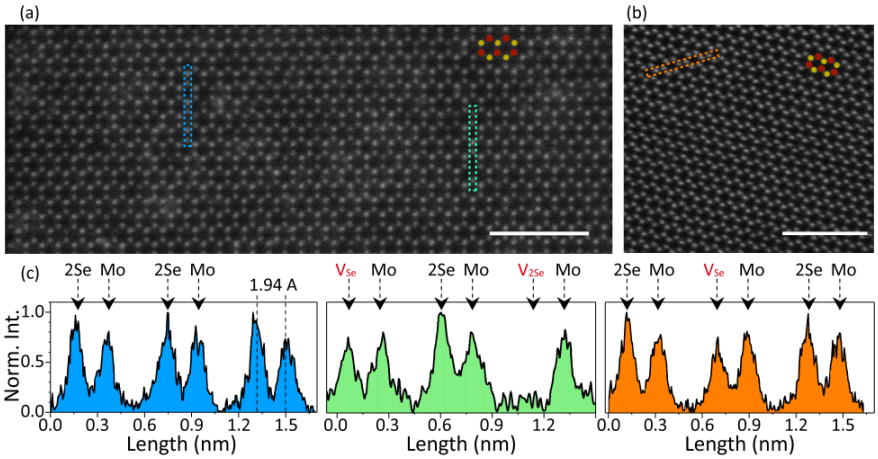

Figure 12, STEM analysis of native point defects. (a,b) High-resolution STEM images of representative CVD-grown and exfoliated $MoSe_2$ monolayer films, respectively. Red and blue circles mark Mo and Se_2 atomic sites, respectively. (c) Intensity profiles across the atomic lines highlighted in (a) and (b). Identical color codes are used in panels (a-c). Using the intensity profile (left profile), the Mo sublattice can be distinguished from the Se_2 sub-lattice. Accordingly, deviation from the reference intensities is used to identify vacancies on CVD-grown (middle profile) and exfoliated (right profile) $MoSe_2$ sample. A few representative V_{Se} and V_{2Se} vacancies are marked on the STEM images.

Using the above criterion, we can count the number of V_{Se} and V_{2Se} vacancies across an imaged area, and we estimated the areal density of vacancies in CVD-grown and exfoliated films. Inspecting several samples from each $MoSe_2$ type showed that the average density of V_{Se} vacancies in CVD-grown and exfoliated films are ~ 1.23×106 μm^{-2} and ~ 0.42×106 μm^{-2}, respectively. We also estimated a density of ~ 0.11×106 μm^{-2} for V_{2Se} vacancies in CVD-grown monolayers. These estimated areal vacancy densities translate into 7.83% and 2.17% Se deficiencies in CVD-grown and exfoliated monolayers, respectively. Indeed, the Se deficiency in CVD-grown films is more than three times larger than that in exfoliated $MoSe_2$ monolayers. Since our alloying approach relies on replacing Se atoms by S atoms, the unoccupied Se sites (i.e., Se vacancies) in starting $MoSe_2$ crystals may serve as atomic sites from which S atoms enter the $MoSe_2$ lattice. Thus, we speculate that the presence of Se vacancies lowers the barrier for the chalcogen substitution and mediates the alloying process. Accordingly, the sulfurization of CVD-grown $MoSe_2$ films with abundant Se vacancies results in $MoS_{2x}Se_{2(1-x)}$ alloys with x values larger than that in exfoliated samples with fewer native Se vacancies.

To obtain further insight into the defect-mediated alloying mechanism, we collaborated with Reed's group at Stanford University to performed density-functional theory (DFT) calculations. In our DFT studies, we consider that S atoms may incorporate into the host lattice of $MoSe_2$ via occupying the pre-existing vacancy sites, which may serve as niches from which the alloying process initiates and further spreads throughout the lattice (Figure 13). However, our STEM analysis showed that the Se deficiency in host $MoSe_2$ monolayers is limited to only 7.83% (in CVD-grown samples). Thus, a sustainable defect-mediated alloying process needs further generation of Se vacancies after the pre-existing vacancies are occupied by S atoms. Our calculations show that the energy barrier for the generation of Se vacancies is larger than the thermal energy provided during the high-temperature alloying process (i.e., KT ≈ 0.12 eV @ 950℃), meaning that the thermal desorption of Se atoms is unlikely. However, our DFT calculations suggest that such an energy barrier can be supplied by the energy released upon the occupation of pre-existing Se vacancies by S atoms, which enables the chalcogen substitution to proceed beyond the level of pre-existing Se deficiencies.

As demonstrated in PL maps, our sulfurization process yields $MoS_{2x}Se_{2(1-x)}$ alloys with spatially uniform compositions across the whole plane of 2D material, suggesting that a diffusion process assists the uniform distribution of S atoms within the plane of host $MoSe_2$ monolayers. To computationally study this phenomenon, we considered (in collaboration with E. Reed at Stanford University) a two-step process in which a sulfur binds to a Se-vacancy site and then diffuses throughout the layer via exchanging position with Se vacancies. To estimate an energy barrier for this process, we performed nudged elastic band (NEB) calculations using DFT calculations [62]. Our estimation indicates that S atoms could be diffusing through the crystal, but the diffusion length (~20 nm/√20 minutes) is not long enough to allow for the widespread sulfurization from a single vacancy site. Thus, a higher vacancy concentration throughout the sample could enhance the incorporation of S into Se vacancy sites and then subsequent diffusion of S atoms, leading to the nearly-complete sulfurization of the sample at elevated temperatures. In addition to Se vacancies, other types of defects such as edge sites (in both CVD-grown and exfoliated films) and nanoscale pinholes (mostly in CVD-grown samples) may also serve as alternative channels for the incorporation of S atoms into the $MoSe_2$ lattice. However, considering the short diffusion length of S atoms, we believe that such alternative channels play secondary roles in the alloying process. In fact, S atoms that enter the host $MoSe_2$ lattice via the edge sites can diffuse to only a short distance from the edges (e.g., 20 nm), restricting the role of edge sites to only a confined region close to the periphery of relatively large $MoSe_2$ films.

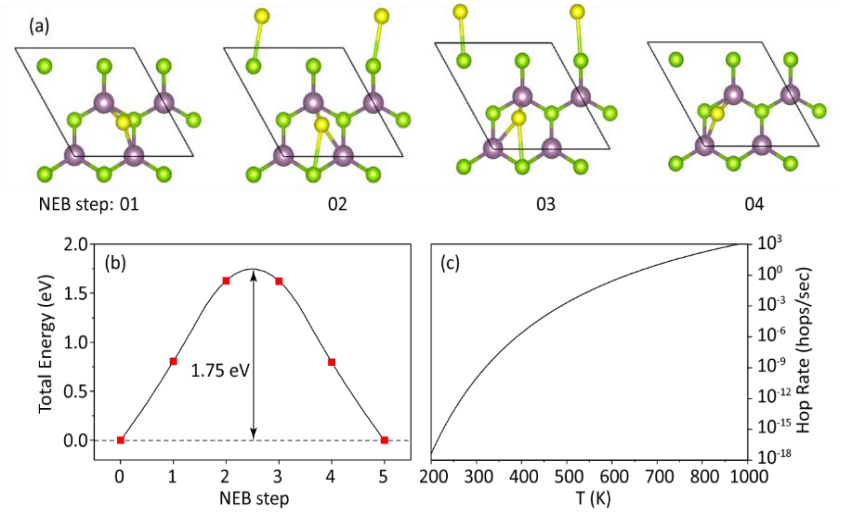

Figure 13, DFT calculation of the vacancy-mediated diffusion. (a) The top view of four intermediate stages used in the NEB calculation of a S atom exchanging places with a Se vacancy. In the 4-formula unit cell of $MoSe_2$, we replace one Se atom by S and remove a neighboring Se atom to create the vacancy to form Mo_4Se_6S. Purple, green, and yellow colors represent Mo, Se, and S, respectively. (b) The NEB energy barrier computed for the exchange of a S atom with a Se vacancy, as shown in the path illustrated in panel (a). Symbols represent computed values, and the line represents a quadratic fit to data points. (c) The temperature-dependent hopping rate computed using the 1.75 eV barrier height shown in panel (b).

In addition to native defects inherited from the synthesis processes of monolayer TMDCs, defects can be deliberately introduced via several techniques including plasma treatment [63], electron-beam irradiation, [64] and ion-beam irradiation [65]. Such artificial defect-generation methods can be employed to further tune the density and type of defects in binary TMDCs, offering an extra level of control over the defect-mediated alloying mechanism that we have studied in this program.

III. Publications and Presentations

III.A. Journal papers

2018

[1] A. E. Dorche, A. H. Hosseinnia, A. A. Eftekhar, and A. Adibi, "Wideband bright-soliton frequency-comb generation at optical telecommunication wavelength in a thin silicon nitride film," Journal of Nanophotonics, vol. 12, no. 4, pp. 046008, 2018.

[2] T. Fan, H. Moradinejad, X. Wu, A. A. Eftekhar, and A. Adibi, "High-Q integrated photonic microresonators on 3c-sic-on-insulator (sicoi) platform," Optics express, vol. 26, no. 20, pp. 25814-25826, 2018.

[3] S. H. S. Mousavi, R. Lemasters, F. Wang, A. E. Dorche, H. Taheri, A. A. Eftekhar, H. Harutyunyan, and A. Adibi, "Phase-matched nonlinear second-harmonic generation in plasmonic metasurfaces," Nanophotonics, 2019.

[4] H. Taghinejad, A. A. Eftekhar, P. M. Campbell, B. Beatty, M. Taghinejad, Y. Zhou, C. J. Perini, H. Moradinejad, W. E. Henderson, and E. V. Woods, "Strain relaxation via formation of cracks in compositionally modulated two-dimensional semiconductor alloys," npj 2D Materials and Applications, vol. 2, 2018.

[5] H. Taghinejad, D. A. Rehn, C. Muccianti, A. A. Eftekhar, M. Tian, T. Fan, X. Zhang, Y. Meng, Y. Chen, and T.-V. Nguyen, "Defect-mediated alloying of monolayer transition-metal dichalcogenides," ACS nano, vol. 12, no. 12, pp. 12795-12804, 2018.

[6] M. Taghinejad, H. Taghinejad, S. T. Malak, H. Moradinejad, E. V. Woods, Z. Xu, Y. Liu, A. A. Eftekhar, T. Lian, and V. V. Tsukruk, "Sharp and tunable crystal/fano-type resonances enabled by out-of-plane dipolar coupling in plasmonic nanopatch arrays," Annalen der Physik, vol. 530, no. 10, pp. 1700395, 2018.

[7] M. Taghinejad, H. Taghinejad, Z. Xu, K.-T. Lee, S. P. Rodrigues, J. Yan, A. Adibi, T. Lian, and W. Cai, "Ultrafast control of phase and polarization of light expedited by hot-electron transfer," Nano letters, vol. 18, no. 9, pp. 5544-5551, 2018.

[8] M. Taghinejad, H. Taghinejad, Z. Xu, Y. Liu, S. P. Rodrigues, K. T. Lee, T. Lian, A. Adibi, and W. Cai, "Hot-electron-assisted femtosecond all-optical modulation in plasmonics," Advanced Materials, vol. 30, no. 9, pp. 1704915, 2018.

[9] Hossein Taghinejad, Ali A. Eftekhar, Ali Adibi, "Lateral and Vertical Heterostructures in Two-dimensional Transition-Metal Dichalcogenides," **Invited review**, Optics material express

Previous years

[10] H. Taghinejad, M. Taghinejad, A. Tarasov, M. Y. Tsai, A. H. Hosseinnia, H. Moradinejad, P. M. Campbell, A. A. Eftekhar, E. M. Vogel, A. Adibi "Resonant light-induced heating in hybrid cavity-coupled 2D transition-metal dichalcogenides," ACS Photonics, 3 (4), pp. 700-707, 2016.

[11] H. Taghinejad, S. H. Shams-Mousavi, Y. Gong, M. Taghinejad, A. A Eftekhar, P. Ajayan, A. Adibi "Lattice plasmon induced large enhancement of excitonic emission in monolayer metal dichalcogenides," Plasmonics, pp.1-7, 2017.

[12] H. Taheri, A. A. Eftekhar, K. Wiesenfeld, and A. Adibi, "Anatomy of phase locking in hyperparametric oscillations based on kerr nonlinearity," IEEE Photonics Journal, 9(3), pp.1-11, 2017.

[13] H. Taheri, P. Del'Haye, A. A. Eftekhar, K. Wiesenfeld, and A. Adibi, "Self-synchronization phenomena in the Lugiato-Lefever equation," Physical Review A, 96(1), p.013828, 2017.

[14] R. Dehghannasiri, M. Soltani, and A. Adibi, "Efficient finite-element formulation for analysis of whispering-gallery-mode optical resonators," JOSA B, 34(10), pp.2259-2265, 2017.

[15] R. Dehghannasiri, A. A. Eftekhar, and A. Adibi, "Raman-like stimulated Brillouin scattering in phononic-crystal-assisted silicon-nitride waveguides," Physical Review A, 96(5), p.053836, 2017.

[16] A. Eshaghian Dorche, S. Abdollahramezani, H. Taheri, A. A. Eftekhar, and A. Adibi, "Extending chip-based Kerr-comb to visible spectrum by dispersive wave engineering," Optics Express, vol. 25, pp. 22362-22374, 2017.

Submitted or In-preparation Refereed Journal Papers

[17] Hesam Moradinejad, Murtaza Askari, Amir H. Atabaki, Zhixuan Xia, Ali A. Eftekhar, and Ali Adibi, "Miniaturized High-Q Silicon Nitride Resonators at Visible Wavelengths," Submitted to optics express (2018).

[18] A. H. Hosseinnia, J. Lavrencik, M. Sodagar, A. A. Eftekhar, S. E. Ralph, and A. Adibi, "Integrated Resonant Modulation in Heterogeneous Silicon on Silicon Nitride Platforms," To be submitted to Optics Express (2019).

[19] T. Fan, X. Wu, A. A. Eftekhar, and A. Adibi, " High-Q Microresonators at visible to IR wavelengths on a 3C-SiC-on-Insulator Platform, "in-preparation for Optics Express.

[20] X. Wu, T. Fan, A. A. Eftekhar, and A. Adibi, "High-Q thermally reconfigurable microresonators a 3C-SiC-on-Insulator platform," In-preparation for Optics Letters

III.B. Refereed Conference Papers

2018

[1] R. Dehghannasiri, H. Moradinejad, T. Fan, A. H. Hosseinnia, A. A. Eftekhar, and A. Adibi, "Integrated optomechanical resonators in double-layer crystalline silicon platforms," in 2018 IEEE Photonics Conference (IPC), IEEE, pp. 1-2, 2018.

[2] A. E. Dorche, A. A. Eftekhar, and A. Adibi, "Kerr-comb generation in a dispersion engineered coupled thin silicon nitride microresonators," in CLEO: QELS_Fundamental Science, Optical Society of America, p. JTu2A. 85, 2018.

[3] A. E. Dorche, A. A. Eftekhar, and A. Adibi, "Wideband kerr-comb near visible spectrum in coupling-engineered thin silicon nitride resonators," in CLEO: Applications and Technology, Optical Society of America, p. JW2A. 33, 2018.

[4] T. Fan, A. A. Eftekhar, and A. Adibi, "High-q microresonators at near-infrared/near visible wavelengths on a 3c-sic-on-insulator (sicoi) platform," in 2018 IEEE Photonics Conference (IPC), IEEE, pp. 1-2, 2018.

[5] T. Fan, H. Moradinejad, X. Wu, A. A. Eftekhar, and A. Adibi, "High Q integrated photonic microresonators on 3c sic-on-insulator platform," in CLEO: Science and Innovations, Optical Society of America, p. SW4A. 2, 2018.

[6] H. Taghinejad, D. Daniel Rehn, A. Eftekhar, X. Zhang, S. Shi, P. Ajayan, E. Reed, and A. Adibi, "Role of native defects in post-synthesis alloying of transition metal dichalcogenides," Bulletin of the American Physical Society, 2019.

[7] H. Taghinejad, A. Eftekhar, P. Campbell, M. Taghinejad, Y. Zhou, E. Reed, E. Vogel, and A. Adibi, "Alloying-induced biaxial strain in ternary alloys of transition-metal dichalcogenides (tmds)(conference presentation)," in Photonic and Phononic Properties of Engineered Nanostructures VIII, International Society for Optics and Photonics, p. 1054112, 2018.

[8] H. Taghinejad, A. Eftekhar, M. Taghinejad, Y. Zhou, E. Reed, and A. Adibi, "Crack formation induced by the post-growth alloying of two-dimensional transition-metal dichalcogenides," in APS Meeting Abstracts, 2018.

[9] H. Taghinejad, A. A. Eftekhar, and A. Adibi, "Lateral heterostructures in two-dimensional transition metal dichaolcogenides for optoelectronic applications (conference presentation)," in Active Photonic Platforms X, International Society for Optics and Photonics, p. 107210L, 2018.

[10] H. Taghinejad, A. A. Eftekhar, and A. Adibi, "Planar heterostructures through selective-area alloying of 2d transition metal dichalcogenide (conference presentation)," in 2D Photonic Materials and Devices, International Society for Optics and Photonics, p. 105340R, 2018.

[11] M. Taghinejad, H. Taghinejad, and A. Adibi, "Ultra-sharp and tunable lattice plasmons in film-coupled metallic nanostructures (conference presentation)," in Photonic and Phononic Properties of Engineered Nanostructures VIII, International Society for Optics and Photonics, p. 105410T, 2018.

[12] T. Fan, H. Taghinejad, A. H. Hosseinnia, H. Moradinejad, A. A. Eftekhar, A. Adibi, “A high-Quality silicon nitride (SiN) platform integrated with two-dimensional (2D) materials,” SPIE OPTO. Feb 2019

[13] T. Fan, H. Moradinejad, X. Wu, A. A. Eftekhar, A. Adibi, “A 3C-SiC-on-oxide (SiCOI) platform enabling high-Q resonators over an octave frequency range from visible to near-infrared,” SPIE OPTO. Feb 2019

Previous years

[14] R. Dehghannasiri, A. A. Eftekhar, and A. Adibi, "Raman-like stimulated Brillouin scattering in SiN waveguides," CLEO: Science and Innovations, pp. SM1E.8, San Jose, CA, 2016.

[15] H. Taheri, P. Del'Haye, A. A. Eftekhar, K. Wiesenfeld, and A. Adibi, "Self-synchronization and phase steps in microresonator-based optical frequency combs," CLEO: Science and Innovations, pp. STu1H.6, San Jose, CA, 2016.

[16] H. Moradinejad, M. Askari, A. H. Atabaki, Z. Xia, A. A. Eftekhar and A. Adibi, "Miniaturized high-Q silicon nitride resonators at visible wavelengths," IEEE Photonics Conference (IPC), Orlando, FL, 2017.

[17] R. Dehghannasiri, A. A. Eftekhar and A. Adibi, “Observation of stimulated Brillouin scattering in Si3N4 waveguides,” IEEE Photonics Conference (IPC), Orlando, FL, 2017.

[18] A. H. Hosseinnia, M. Sodagar, H. Moradinejad, T. Fan, A. A. Eftekhar and A. Adibi, “High-speed active devices integrated in hybrid silicon on silicon nitride platform,” Conference on Lasers and Electro-Optics (CLEO), San Jose, CA, 2017.

[19] H. Taghinejad, M. Taghinejad, A. Tarasov, T. Fan, A. A. Eftekhar, E. M. Vogel, A. Adibi “Strong light enhancement and confinement in two-dimensional transition metal dichalcogenides,” SPIE Photonics West, San Francisco, CA, 2017.

[20] H. Taghinejad, M. Taghinejad, A. Tarasov, A. H. Hosseinnia, H. Moradinejad, A. A. Eftekhar, E. Vogel, and A. Adibi, “Enhancement of light-2D material interaction envisioned for energy harvesting applications,” Conference on Lasers and Electro-Optics (CLEO), San Jose, CA, 2017.

[21] M. Taghinejad, H. Taghinejad, H. Moradinejad, A. A. Eftekhar, and Ali Adibi, "A spectroscopic ellipsometry demonstration of ultrasharp subradiant plasmons," META'17 Incheon, South Korea, 2017.

[22] Fan, T., Taghinejad, H., Eftekhar, A.A. and Adibi, A. "Light-matter interaction in 2D material heterostructures," SPIE Photonics West Meeting, San Francisco, CA, 2017.

[23] T. Fan, H. Moradinejad, X. Wu, A. A. Eftekhar, and A. Adibi, "Crystalline silicon carbide on insulator (SCOI) material platform for integrated photonic applications," accepted in SPIE Photonics West, San Francisco, CA, 2018.

[24] H. Taghinejad, A. A. Eftekhar, M. Taghinejad, and A. Adibi, "Alloying-induced biaxial strain in ternary alloys of transition-metal dichalcogenides (TMDs)," accepted for presentation in SPIE Photonics West, San Francisco, CA, 2018.

[25] M. Taghinejad, H. Taghinejad, and A. Adibi, "Ultra-sharp and tunable lattice plasmons in film-coupled metallic nanostructures," accepted for presentation in SPIE Photonics West, San Francisco, CA, 2018.

Accepted Conference Papers

[24] T. Fan, X. Wu, A. A. Eftekhar, and A. Adibi, " Record-High-Q Microresonators from 650 nm to 1550 nm Wavelengths on a 3C-SiC-on-Insulator Platform, "in CLEO: Science and Innovations, Optical Society of America, 2019.

[25] X. Wu, T. Fan, A. A. Eftekhar, and A. Adibi, "High-Q microresonators integrated with microheaters on a 3C-SiC-on-Insulator platform," in CLEO: Science and Innovations, Optical Society of America, 2019.

[26] A. E. Dorche, A. A. Eftekhar, and A. Adibi, "Near-visible bright-soliton Kerr comb generation in dispersion-engineered lithium niobate coupled optical microresonators," in CLEO: Science and Innovations, Optical Society of America, 2019.

III.C. Invited Presentations and Keynotes

2018

[1] A. H. Hosseinnia, N. Sodagar, H. Moradinejad, T. Fan, A. A. Eftekhar, and A. Adibi, "Hybrid Material Platforms for Low-power, High-speed, and Miniaturized Integrated Photonic Devices and Systems." **Invited Keynote Talk** fpr presentation in Optics and Photonics Conference, Philadelphia, PA, October 2018.

[2] H. Taghinejad, A. A. Eftekhar, and A. Adibi, "Planar heterostructures through selective-area alloying of 2D transition metal dichalcogenide," **Invited** for presentation in SPIE Photonics West, San Francisco, CA, 2018.

[3] H. Taghinejad, A. A. Eftekhar, A. Adibi, "Lateral heterostructures in two-dimensional transition metal dichalcogenides for optoelectronic applications." **Invited** for presentation in SPIE Optics and Photonics, San Diego, CA, August 2018.

[4] A. H. Hosseinnia, T. Fan, H. Moradinejad, N. Sodagar, S. Taghavi, A. A. Eftekhar, and A. Adibi, "Low-power High-speed Resonance-based Integrated Photonic Modulators." **Invited** for presentation in IEEE Photonics Conference (IPC), Reston, VA, October 2018.

[5] A. H. Hosseinnia, N. Sodagar, H. Moradinejad, T. Fan, A. A. Eftekhar, and A. Adibi, "Hybrid Material Platforms for Reconfigurable Integrated Nanophotonics, **Invited** for presentation in Stegeman Symposium." Orlando, FL, March 2018.

[6] A. H. Hosseinnia, N. Sodagar, H. Moradinejad, T. Fan, A. A. Eftekhar, and A. Adibi, "Hybrid Material Platforms for Low-power, High-speed, and Miniaturized Integrated Nanophotonic Devices and Systems." **Invited** seminar talk for presentation in Samsung USA, San Jose, CA, August 2018.

[7] A. Adibi, "Hybrid Material and Device Platforms for Reconfigurable Integrated Nanophotonics." **Invited** seminar talk for presentation in Georgia Tech Lorraine, Metz, France, June 2018.

[8] A. Adibi, "Hybrid Material and Device Platforms for Reconfigurable Integrated Nanophotonics." **Invited** seminar talk for presentation in Aachen University, Aachen, Germany, June 2018.

[9] A. Adibi, "Hybrid Material and Device Platforms for Reconfigurable Integrated Nanophotonics." **Invited** seminar talk for presentation in Institute of Materials for Electronics and Magnetism (IMEM-CNR), Parma, Italy, June 2018.

[10] H. Taghinejad, "Synthesis of lateral heterostructures of transition-metal dichalcogenides via spatially-controlled alloying," Invited, SPIE OPTO. Feb 2019

Previous years

[11] A. Adibi, "Integrated nanophotonic structures for optical computing," **Invited** for Presentation in Beyond CMOS Computing Workshop, Baltimore, MD, February 2016.

[12] A. Adibi, "Hybrid material platforms for reconfigurable integrated photonic structures", **Invited** for Presentation in Reconfigurable Electronic Workshop, Arlington, VA, May 2016.

[13] A. H. Hosseinnia, H. Moradinejad, M. Sodagar, A. A. Eftekhar, and A. Adibi, "Hybrid CMOS-compatible material and device platform for integrated nanophotonics," **Invited** for Presentation in CLEO: Science and Innovations, San Jose, CA, June 2016.

[14] S. H. Shams Mousavi, H. Taghinejad, M. Taghinejad, A. A. Eftekhar, and A. Adibi, "Strong light-matter interaction in two-dimensional transition metal dichalcogenides through integration with plasmonic nanoantenna arrays," **Invited** for Presentation in META Conference, Malaga, Spain, July 2016.

[15] S. H. Shams-Mousavi, H. Taghinejad, M. Taghinejad, A. A. Eftekhar and A. Adibi, "Strong light-matter interaction through mode engineering in plasmonic nanoantenna arrays," **Invited** for Presentation in Progress in Electromagnetic Research Symposium (PIERS), Shanghai, China, July 2016.

[16] A. Adibi "Hybrid material and device platforms for reconfigurable integrated nanophotonics," **Invited** Seminar Talk, Jet Propulsion Laboratory, Pasadena, CA January 2016.

[17] A. Adibi "Hybrid material and device platforms for reconfigurable integrated nanophotonics," **Invited** Seminar Talk, University of Washington, Seattle, WA, January 2016.

[18] H. Maoradinejad, A. H. Hosseinnia, T. Fan, M. Sodagar, A. A. Eftekhar, and A. Adibi, "Hybrid multi-layer integrated nanophotonics materials and devices," **Invited** for Presentation in SPIE Optics and Photonics, San Diego, CA, August 2016.

[19] H. Taghinejad, S. H. Shams Mousavi, T. Fan, M. Taghinejad, A. A. Eftekhar, and A. Adibi, "Plasmonic enhancement of light-matter interaction in planar materials," **Invited** for presentation in META 2017 Conference, Seoul, South Korea, 2017.

[20] H. Moradinejad, T. Fan, A. H. Hosseinnia, M. Sodagar, S. Taghavi, A. A. Eftekhar, and A. Adibi, "Optical modulation in hybrid integrated nanophotonic platforms," **Invited** for presentation in IEEE Summer Topicals Meeting, San Juan, Puerto Rico, 2017.

References:

[1] A. E. Dorche, A. A. Eftekhar, and A. Adibi, “Near-visible bright-soliton Kerr comb generation in dispersion-engineered lithium niobate coupled optical microresonators,” in CLEO: Science and Innovations, Optical Society of America, 2019.

[2] A. E. Dorche, A. H. Hosseinnia, A. A. Eftekhar, and A. Adibi, “Wideband bright-soliton frequency-comb generation at optical telecommunication wavelength in a thin silicon nitride film,” Journal of Nanophotonics, vol. 12, no. 4, pp. 046008, 2018.

[3] T. Fan, H. Moradinejad, X. Wu, A. A. Eftekhar, and A. Adibi, “High-Q integrated photonic microresonators on 3c-sic-on-insulator (sicoi) platform,” Optics express, vol. 26, no. 20, pp. 25814-25826, 2018.

[4] T. Fan, H. Moradinejad, X. Wu, A. A. Eftekhar, A. Adibi, “A 3C-SiC-on-oxide (SiCOI) platform enabling high-Q resonators over an octave frequency range from visible to near-infrared,” SPIE OPTO. Feb 2019

[5] S. H. S. Mousavi, R. Lemasters, F. Wang, A. E. Dorche, H. Taheri, A. A. Eftekhar, H. Harutyunyan, and A. Adibi, “Phase-matched nonlinear second-harmonic generation in plasmonic metasurfaces,” Nanophotonics, 2019.

[6] M. Taghinejad, H. Taghinejad, S. T. Malak, H. Moradinejad, E. V. Woods, Z. Xu, Y. Liu, A. A. Eftekhar, T. Lian, and V. V. Tsukruk, “Sharp and tunable crystal/fano-type resonances enabled by out-of-plane dipolar coupling in plasmonic nanopatch arrays,” Annalen der Physik, vol. 530, no. 10, pp. 1700395, 2018.

[7] M. Taghinejad, H. Taghinejad, Z. Xu, K.-T. Lee, S. P. Rodrigues, J. Yan, A. Adibi, T. Lian, and W. Cai, “Ultrafast control of phase and polarization of light expedited by hot-electron transfer,” Nano letters, vol. 18, no. 9, pp. 5544-5551, 2018.

[8] M. Taghinejad, H. Taghinejad, Z. Xu, Y. Liu, S. P. Rodrigues, K. T. Lee, T. Lian, A. Adibi, and W. Cai, “Hot-electron-assisted femtosecond all-optical modulation in plasmonics,” Advanced Materials, vol. 30, no. 9, pp. 1704915, 2018.

[9] H. Taghinejad, A. A. Eftekhar, P. M. Campbell, B. Beatty, M. Taghinejad, Y. Zhou, C. J. Perini, H. Moradinejad, W. E. Henderson, and E. V. Woods, “Strain relaxation via formation of cracks in compositionally modulated two-dimensional semiconductor alloys,” npj 2D Materials and Applications, vol. 2, 2018.

[10] H. Taghinejad, D. A. Rehn, C. Muccianti, A. A. Eftekhar, M. Tian, T. Fan, X. Zhang, Y. Meng, Y. Chen, and T.-V. Nguyen, “Defect-mediated alloying of monolayer transition-metal dichalcogenides,” ACS nano, vol. 12, no. 12, pp. 12795-12804, 2018.

[11] R. Dehghannasiri, H. Moradinejad, T. Fan, A. H. Hosseinnia, A. A. Eftekhar, and A. Adibi, "Integrated optomechanical resonators in double-layer crystalline silicon platforms," in 2018 IEEE Photonics Conference (IPC), IEEE, pp. 1-2, 2018.

[12] R. Dehghannasiri, A. A. Eftekhar and A. Adibi, “Observation of stimulated Brillouin scattering in Si3N4 waveguides,” IEEE Photonics Conference (IPC), Orlando, FL, 2017.

[13] H. Morkoç, S. Strite, G. B. Gao, M. E. Lin, B. Sverdlov, and M. Burns, "Large-band-gap SiC, III-V nitride, and II-VI ZnSe-based semiconductor device technologies," J. Appl. Phys. 76(3), 1363–1398 (1994).

[14] 5. R. Adair, L. L. Chase, and S. A. Payne, "Nonlinear refractive index of optical crystals," Phys. Rev. B 39(5), 3337–3350 (1989).

[15] G. L. DesAutels, C. Brewer, M. Walker, S. Juhl, M. Finet, S. Ristich, M. Whitaker, and P. Powers, "Femtosecond laser damage threshold and nonlinear characterization in bulk transparent SiC materials," J. Opt. Soc. Am. B 25(1), 60-66 (2008).

[16] X. Lu, J. Y. Lee, S. Rogers, and Q. Lin, "Optical Kerr nonlinearity in a high-Q silicon carbide microresonator," Opt. Express 22(25), 30826-30832 (2014).

[17] J. Bravo-Abad, A. Rodriguez, P. Bermel, S. G. Johnson, J. D. Joannopoulos, and M. Soljacic, "Enhanced nonlinear optics in photonic-crystal microcavities," Opt. Express 15(24), 16161-16176 (2007).

[18] P. Del'Haye, A. Schliesser, O. Arcizet, T. Wilken, R. Holzwarth, and T. J. Kippenberg, "Optical frequency comb generation from a monolithic microresonator," Nature 450(7173), 1214–1217 (2007).

[19]W. F. Koehl, B. B. Buckley, F. J. Heremans, G. Calusine, and D. D. Awschalom, "Room temperature coherent control of defect spin qubits in silicon carbide," Nature 479(7371), 84–87 (2011).

[20] A. L. Falk, B. B. Buckley, G. Calusine, W. F. Koehl, V. V. Dobrovitski, A. Politi, C. A. Zorman, P. X. L. Feng, and D. D. Awschalom, "Polytype control of spin qubits in silicon carbide," Nat. Commun. 4, 1819 (2013).

[21] S. Castelletto, B. C. Johnson, V. Ivády, N. Stavrias, T. Umeda, A. Gali, and T. Ohshima, " A silicon carbide room-temperature single-photon source," Nat. Mater. 13, 151–156 (2013).

[22] A. Lohrmann, N. Iwamoto, Z. Bodrog, S. Castelletto, T. Ohshima, T. J. Karle, A. Gali, S. Prawer, J. C. McCallum, and B. C. Johnson, "Single-photon emitting diode in silicon carbide," Nat. Commun. 6, 7783 (2015).

[23] H. Morkoç, S. Strite, G. B. Gao, M. E. Lin, B. Sverdlov, and M. Burns, "Large-band-gap SiC, III-V nitride, and II-VI ZnSe-based semiconductor device technologies," J. Appl. Phys. 76(3), 1363–1398 (1994).

[24] M. Bosi, G. Attolini, M. Negri, C. Ferrari, E. Buffagni, C. Frigeri, M. Calicchio, B. Pécz, F. Riesz, I. Cora, Z. Osváth, L. Jiang, and G. Borionetti, "Defect structure and strain reduction of 3C-SiC/Si layers obtained with the use of a buffer layer and methyltrichlorosilane addition," Cryst. Eng. Comm. 18(15), 2770–2779 (2016).

[25] X. Lu, J. Lee, P. Feng, Q. Lin, X. Lu, J. Y. Lee, and P. X.-L. Feng," A silicon carbide microdisk resonator," Opt. Lett. 38(8), 1304–1306 (2013).

[26] B.-S. Song, S. Yamada, T. Asano, and S. Noda, "Demonstration of two-dimensional photonic crystals based on silicon carbide," Opt. Express 19(12), 11084-11089 (2011).

[27] S. Yamada, B. S. Song, T. Asano, and S. Noda, "Silicon carbide-based photonic crystal nanocavities for ultra-broadband operation from infrared to visible wavelengths," Appl. Phys. Lett. 99(20), 201102 (2011).

[28] S. Yamada, B.-S. Song, T. Asano, and S. Noda, "Experimental investigation of thermo-optic effects in SiC and Si photonic crystal nanocavities," Opt. Lett. 36(20), 3981-3983 (2011).

[29] S. Yamada, B. Song, J. Upham, T. Asano, Y. Tanaka, and S. Noda, "Suppression of multiple photon absorption in a SiC photonic crystal nanocavity operating at 155 μm," Opt. Express 20(14), 14789-14796 (2012).

[30] J. Cardenas, M. Zhang, C. T. Phare, S. Y. Shah, C. B. Poitras, B. Guha, and M. Lipson, "High Q SiC microresonators," Opt. Express 21(14), 16882-16887 (2013).

[31] M. Radulaski, T. M. Babinec, S. Buckley, A. Rundquist, J. Provine, K. Alassaad, G. Ferro, and J. Vučković, "Photonic crystal cavities in cubic (3C) polytype silicon carbide films," Opt. Express 21(26), 32623-32629 (2013).

[32] A. P. Magyar, D. Bracher, J. C. Lee, I. Aharonovich, and E. L. Hu, "High quality SiC microdisk resonators fabricated from monolithic epilayer wafers," Appl. Phys. Lett. 104(5), 051109 (2014).

[33] X. Lu, J. Y. Lee, P. X. Feng, and Q. Lin, "High Q silicon carbide microdisk resonator," Appl. Phys. Lett. 104(18), 181103 (2014).

[34] F. Martini, and A. Politi, "Linear integrated optics in 3C silicon carbide," Opt. Express 25(10), 10735-10742 (2017).

[35] L. D. Cioccio, F. Letertre, Y. L. Tiec, A. M. Papon, C. Jaussaud, and M. Bruel, "Silicon carbide on insulator formation by the Smart-Cut process," Mater. Sci. Eng. B46(1-3), 349–356 (1997).

[36] J. Cardenas, M. Yu, Y. Okawachi, C. B. Poitras, R. K. W. Lau, A. Dutt, A. L. Gaeta, and M. Lipson, "Optical nonlinearities in high-confinement silicon carbide waveguides," Opt. Lett. 40(17), 4138–4141 (2015).

[37] H. Moradinejad, A. H. Atabaki, A. H. Hosseinnia, A. A. Eftekhar, and A. Adibi, "Double-layer crystalline silicon on insulator material platform for integrated photonic applications," IEEE Photonics J. 6(6), 1-8 (2014).

[38] A. H. Hosseinnia, A. H. Atabaki, A. A. Eftekhar, and A. Adibi, "High-quality silicon on silicon nitride integrated optical platform with an octave-spanning adiabatic interlayer coupler," Opt. Express 23(23), 30297-30307 (2015).

[39] T. Fan, X. Wu, A. A. Eftekhar, and A. Adibi, " Record-High-Q Microresonators from 650 nm to 1550 nm Wavelengths on a 3C-SiC-on-Insulator Platform," in CLEO: Science and Innovations, Optical Society of America, 2019.

[40] M. Bosi, C. Ferrari, D. Nilsson, and P. J. Ward, "3C-SiC carbonization optimization and void reduction on misoriented Si substrates: from a research reactor to a production scale reactor," Cryst. Eng. Comm. 18(39), 7478–7486 (2016).

[41] X. Ji, F. A. S. Barbosa, S. P. Roberts, A. Dutt, J. Cardenas, Y. Okawachi, A. Bryant, A. L. Gaeta, and M. Lipson, "Ultra-low-loss on-chip resonators with sub-milliwatt parametric oscillation threshold," Optica 4(6), 619-624 (2017).

[42] J. Cardenas, M. Zhang, C. T. Phare, S. Y. Shah, C. B. Poitras, B. Guha, and M. Lipson, "High Q SiC microresonators," Opt. Express 21(14), 16882-16887 (2013).

[43] X. Lu, J. Y. Lee, P. X. Feng, and Q. Lin, "High Q silicon carbide microdisk resonator," Appl. Phys. Lett. 104(18), 181103 (2014).

[44] T. Fan, H. Moradinejad, X. Wu, A. A. Eftekhar, and A. Adibi, "High-Q integrated photonic microresonators on 3C-SiC-on-insulator (SiCOI) platform," Optics express, vol. 26, no. 20, pp. 25814-25826, 2018.

[45] T. Fan, X. Wu, A. A. Eftekhar, and A. Adibi, " Record-High-Q Microresonators from 650 nm to 1550 nm Wavelengths on a 3C-SiC-on-Insulator Platform," in CLEO: Science and Innovations, Optical Society of America, 2019.

[46] X. Wu, T. Fan, A. A. Eftekhar, and A. Adibi, "High-Q microresonators integrated with microheaters on a 3C-SiC-on-Insulator platform," in CLEO: Science and Innovations, Optical Society of America, 2019.

[47] Duan, X. D.; Wang, C.; Fan, Z.; Hao, G. L.; Kou, L. Z.; Halim, U.; Li, H. L.; Wu, X. P.; Wang, Y. C.; Jiang, J. H.; Pan, A. L.; Huang, Y.; Yu, R. Q.; Duan, X. F. Synthesis of $WS_{2x}Se_{2-2x}$ Alloy Nanosheets with Composition-Tunable Electronic Properties. Nano Lett 2016, 16, 264-269..

[48] Li, H. L.; Duan, X. D.; Wu, X. P.; Zhuang, X. J.; Zhou, H.; Zhang, Q. L.; Zhu, X. L.; Hu, W.; Ren, P. Y.; Guo, P. F.; Ma, L.; Fan, X. P.; Wang, X. X.; Xu, J. Y.; Pan, A. L.; Duan, X. F. Growth of Alloy $MoS_{2x}Se_{2(1-x)}$ Nanosheets with Fully Tunable Chemical Compositions and Optical Properties. J Am Chem Soc 2014, 136, 3756-3759

[49] Mahjouri-Samani, M.; Lin, M. W.; Wang, K.; Lupini, A. R.; Lee, J.; Basile, L.; Boulesbaa, A.; Rouleau, C. M.; Puretzky, A. A.; Ivanov, I. N.; Xiao, K.; Yoon, M.; Geohegan, D. B. Patterned Arrays of Lateral Heterojunctions Within Monolayer Two-Dimensional Semiconductors. Nat Commun 2015, 6, 7749.

[50] Taghinejad, H.; Eftekhar, A. A.; Campbell, P. M.; Beatty, B.; Taghinejad, M.; Zhou, Y.; Perini, C. J.; Moradinejad, H.; Henderson, W. E.; Woods, E. V.; Zhang, Z.; Ajayan, P. M.; Reed, E. J.; Vogel, E. M.; Adibi, A. Strain Relaxation via Formation of Cracks in Compositionally Modulated Two-Dimensional Semiconductor Alloys. Npj 2d Mater Appl 2018, 2, 1-8.

[51] H. Taghinejad, A. A. Eftekhar, P. M. Campbell, B. Beatty, M. Taghinejad, Y. Zhou, C. J. Perini, H. Moradinejad, W. E. Henderson, and E. V. Woods, “Strain relaxation via formation of cracks in compositionally modulated two-dimensional semiconductor alloys,” npj 2D Materials and Applications, vol. 2, 2018.

[52] I.N., Sneddon, and H. A. Elliot. "The opening of a Griffith crack under internal pressure." Quarterly of Applied Mathematics 4.3 (1946): 262-267.

[53] Yin, H. Q.; Qi, H. J.; Fan, F. F.; Zhu, T.; Wang, B. L.; Wei, Y. J. Griffith Criterion for Brittle Fracture in Graphene. Nano Lett 2015, 15, 1918-1924.

[54] Liu, H. J.; Zheng, H.; Yang, F.; Jiao, L.; Chen, J. L.; Ho, W. K.; Gao, C. L.; Jia, J. F.; Xie, M. H. Line and Point Defects in $MoSe_2$ Bilayer Studied by Scanning Tunneling Microscopy and Spectroscopy. ACS Nano 2015, 9, 6619-6625;

[55] Zhou, W.; Zou, X. L.; Najmaei, S.; Liu, Z.; Shi, Y. M.; Kong, J.; Lou, J.; Ajayan, P. M.; Yakobson, B. I.; Idrobo, J. C. Intrinsic Structural Defects in Monolayer Molybdenum Disulfide. Nano Lett 2013, 13, 2615-2622;

[56] Hong, J. H.; Hu, Z. X.; Probert, M.; Li, K.; Lv, D. H.; Yang, X. N.; Gu, L.; Mao, N. N.; Feng, Q. L.; Xie, L. M.; Zhang, J.; Wu, D. Z.; Zhang, Z. Y.; Jin, C. H.; Ji, W.; Zhang, X. X.; Yuan, J.; Zhang, Z. Exploring Atomic Defects in Molybdenum Disulphide Monolayers. Nat Commun 2015, 6, 6293

[57] Lu, C. P.; Li, G. H.; Mao, J. H.; Wang, L. M.; Andrei, E. Y. Bandgap, Mid-Gap States, and Gating Effects in MoS_2. Nano Lett 2014, 14, 4628-4633.

[58] Li, X. F.; Puretzky, A. A.; Sang, X. H.; Santosh, K. C.; Tian, M. K.; Ceballos, F.; Mahjouri-Samani, M.; Wang, K.; Unocic, R. R.; Zhao, H.; Duscher, G.; Cooper, V. R.; Rouleau, C. M.; Geohegan, D. B.; Xiao, K. Suppression of Defects and Deep Levels Using Isoelectronic Tungsten Substitution in Monolayer $MoSe_2$. Adv Funct Mater 2017, 27, 1603850.

[59] Tongay, S.; Suh, J.; Ataca, C.; Fan, W.; Luce, A.; Kang, J. S.; Liu, J.; Ko, C.; Raghunathanan, R.; Zhou, J.; Ogletree, F.; Li, J. B.; Grossman, J. C.; Wu, J. Q. Defects Activated Photoluminescence in Two-Dimensional Semiconductors: Interplay Between Bound, Charged, and Free Excitons. Sci Rep-Uk 2013, 3, 2657.

[60] Surrente, A.; Dumcenco, D.; Yang, Z.; Kuc, A.; Jing, Y.; Heine, T.; Kung, Y. C.; Maude, D. K.; Kis, A.; Plochocka, P. Defect Healing and Charge Transfer-Mediated Valley Polarization in $MoS_2/MoSe_2/MoS_2$ Trilayer van der Waals Heterostructures. Nano Lett 2017, 17, 4130-4136.

[61] Tongay, S.; Suh, J.; Ataca, C.; Fan, W.; Luce, A.; Kang, J. S.; Liu, J.; Ko, C.; Raghunathanan, R.; Zhou, J.; Ogletree, F.; Li, J. B.; Grossman, J. C.; Wu, J. Q. Defects Activated Photoluminescence in Two-Dimensional Semiconductors: Interplay Between Bound, Charged, and Free Excitons. Sci Rep-Uk 2013, 3, 2657.

[62] G. Henkelman, B P. Uberuaga, and H. Jónsson. "A climbing image nudged elastic band method for finding saddle points and minimum energy paths." The Journal of chemical physics 113.22 (2000): 9901-9904.

[63] Chen, M.; Nam, H.; Wi, S.; Ji, L.; Ren, X.; Bian, L.; Lu, S.; Liang, X. Stable Few-Layer MoS_2 Rectifying Diodes Formed by Plasma-Assisted Doping. Appl Phys Lett 2013, 103, 142110.

[64] Parkin, W. M.; Balan, A.; Liang, L. B.; Das, P. M.; Lamparski, M.; Naylor, C. H.; Rodríguez-Manzo, J. A.; Johnson, A. T. C.; Meunier, V.; Drndic, M. Raman Shifts in Electron-Irradiated Monolayer MoS_2. ACS Nano 2016, 10, 4134-4142.

[65] Madaub, L.; Ochedowski, O.; Lebius, H.; Ban-d'Etat, B.; Naylor, C. H.; Johnson, A. T. C.; Kotakoski, J.; Schleberger, M. Defect Engineering of Single- and Few-Layer MoS_2 by Swift Heavy Ion Irradiation. 2d Mater 2016, 4, 015034.